TURUN
YLIOPISTO
UNIVERSITY
OF TURKU

EVALUATION OF DIGITAL PET/CT SYSTEM FOR MYOCARDIAL PERFUSION IMAGING

Reetta Siekkinen

TURUN YLIOPISTON JULKAISUJA – ANNALES UNIVERSITATIS TURKUENSIS
SARJA – SER. D OSA – TOM. 1734 | MEDICA – ODONTOLOGICA | TURKU 2023

TURUN
YLIOPISTO
UNIVERSITY
OF TURKU

EVALUATION OF DIGITAL PET/CT SYSTEM FOR MYOCARDIAL PERFUSION IMAGING

Reetta Siekkinen

TURUN YLIOPISTON JULKAISUJA – ANNALES UNIVERSITATIS TURKUENSIS
SARJA – SER. D OSA – TOM. 1734 | MEDICA – ODONTOLOGICA | TURKU 2023

University of Turku

Faculty of Medicine
Medical Physics and Engineering
Doctoral Programme in Clinical Research
Turku PET Centre

Supervised by

Docent, Jarmo Teuho
Turku PET Centre
Turku University Hospital
University of Turku
Turku, Finland

Professor, Mika Teräs
Department of Medical Physics
Institute of Biomedicine
Turku University Hospital
University of Turku
Turku, Finland

Professor, Antti Saraste
Department of Cardiology
Turku Heart Centre
Turku PET Centre
Turku University Hospital
University of Turku
Turku, Finland

Reviewed by

Professor, Paul Marsden
School of Biomedical Engineering &
Imaging Sciences
King's College London
London, United Kingdom

Docent, Mikko Hakulinen
Diagnostic Imaging Center
Kuopio University Hospital
Kuopio, Finland

Opponent

Professor, Ronald Boellaard
Department of Nuclear Medicine and PET Research
VU University Medical Center
Amsterdam, the Netherlands

The originality of this publication has been checked in accordance with the University of Turku quality assurance system using the Turnitin OriginalityCheck service.

ISBN 978-951-29-9419-9 (PRINT)
ISBN 978-951-29-9420-5 (Online)
ISSN 0355-9483 (Print)
ISSN 2343-3213 (Online)
Painosalama, Turku, Finland 2023

UNIVERSITY OF TURKU
Faculty of Medicine
Medical Physics and Engineering
Turku PET Centre
REETTA SIEKKINEN: Evaluation of Digital PET/CT System for Myocardial Perfusion Imaging
Doctoral Dissertation, 122 pp.
Doctoral Programme in Clinical Research
September 2023

ABSTRACT

Myocardial perfusion imaging (MPI) with Positron Emission Tomography (PET) allows quantitative measurements of absolute myocardial blood flow (MBF). PET system count-rate capabilities, reconstruction techniques, and other technical factors may influence MBF quantification reproducibility and accuracy.

In this thesis the aims were to evaluate the effect of different reconstruction parameters on [^{15}O]H_2O MPI using a flow phantom and clinical retrospective data from patients who had undergone [^{15}O]H_2O MPI for suspected obstructive coronary artery disease. Also, the digital and analog PET system count-rate capabilities were assessed in high count-rate studies. Finally, the aim was to establish the contribution of technical factors on quantitative reproducibility and accuracy on two digital PET systems.

The different reconstruction parameters resulted in a 7% relative error with the image-derived flow values compared to the reference flow values in phantom studies. Similar differences were measured in MBF values in patients. Also, different reconstruction algorithms resulted in similar classification of myocardial ischemia in 99% of the subjects. The digital PET resulted in 12.8 Mcps total prompts and 0.47 Mcps trues, and the analog PET in 6.85 Mcps total prompts and 1.15 Mcps trues with the highest injected activities. The modelled flow values were reproducible on digital PET systems but future studies need to be conducted to develop a standardized and repeatable bolus injection protocol.

The results of these studies showed that the digital PET system can be reliably used in MPI in terms of system count-rate capabilities and novel reconstruction techniques with small contribution from technical factors. The findings offer a basis for assessing reproducibility in MPI in multi-center studies.

KEYWORDS: myocardial perfusion imaging, positron emission tomography, reconstruction, hybrid imaging, myocardial blood flow, flow phantom

TURUN YLIOPISTO
Lääketieteellinen tiedekunta
Lääketieteellinen fysiikka ja tekniikka
Turun PET-keskus
REETTA SIEKKINEN: Digitaalisen PET/TT-laitteiston arviointi sydänlihas-perfuusiokuvantamiseen
Väitöskirja, 122 s.
Turun kliininen tohtoriohjelma
Syyskuu 2023

TIIVISTELMÄ

Positroniemissiotomografialla (PET) toteutettava [^{15}O]H_2O-sydänlihasperfuusio-kuvantaminen mahdollistaa sydänlihaksen verenvirtauksen absoluuttisten arvojen määrittämisen. PET-laitteiston suorituskyky, rekonstruktiotekniikat sekä muut tekniset muuttujat voivat kuitenkin vaikuttaa verenvirtauksen laskennan toistettavuuteen ja tarkkuuteen.

Tässä tutkielmassa tavoitteena oli arvioida eri rekonstruktioparametrien vaikutusta mitattuun verenvirtaukseen käyttäen virtausfantomia sekä retrospektiivistä potilasaineistoa. Lisäksi arvioitiin analogisen ja digitaalisen PET-laitteiston suorituskykyä korkeilla aktiivisuuksilla. Lopuksi tavoitteena oli arvioida teknisten muuttujien vaikutusta laskennalliseen toistettavuuteen ja tarkkuuteen kahdella digitaalisella PET-laitteistolla.

Virtausparametrien suhteellinen ero oli maksimissaan 7 % eri rekonstruktio-parametreilla sekä virtausfantomilla että potilailla, joita tutkittiin ahtauttavan sepelvaltimotaudin epäilyn vuoksi. Lisäksi, sydänlihasiskemialuokittelu oli samanlainen 99 % potilaista eri rekonstruktioilla. Digitaalisen PET-laitteiston kokonaishavaintojen määrä oli 12.8 Mcps ja todellisten havaintojen määrä 0.47 Mcps suurimmalla injisoidulla aktiivisuudella. Analogisella laitteistolla määrät olivat 6.85 Mcps ja 1.15 Mcps. Mallinnetut virtausarvot olivat toistettavia digitaalisilla PET-laitteistoilla, mutta tulevaisuudessa mittaukset vaativat standardoidun ja toistettavan injektio-protokollan.

Näiden tutkimusten tulokset osoittavat, että digitaalisen PET-laitteistoja voidaan luotettavasti käyttää sydänlihasperfuusion kuvantamiseen, kun on arvioitu laitteiston suorituskykyä ja uusien rekonstruktiotekniikoita vuoksi. Lisäksi, näiden tutkimusten pohjalta voidaan tulevaisuudessa arvioida absoluuttisen sydänlihaksen veren-virtauksen toistettavuutta monikeskustutkimuksissa.

AVAINSANAT: sydänlihasperfuusiokuvantaminen, positroniemissiotomografia, rekonstruktio, hybridikuvantaminen, sydänlihaksen verenvirtaus, virtausfantomi

Table of Contents

Abbreviations

MPI	Myocardial Perfusion Imaging
PET	Positron Emission Tomography
MBF	Myocardial Blood Flow
BSREM	Block Sequential Regularized Expectation Maximization
CAD	Coronary Artery Disease
MFR	Myocardial Flow Reserve
CT	Computed Tomography
SPECT	Single Photon Emission Computerized Tomography
MRI	Magnetic Resonance Imaging
EANM	European Association of Nuclear Medicine
LOR	Line-of-Response
P	Prompts
T	Trues
R	Randoms
S	Scatter
NECR	Noise-Equivalent-Count-Rates
SNR	Signal-to-Noise Ratio
FOV	Field-of-View
PMT	Photomultiplier Tube
BGO	Bismuth Germanate
TOF	Time-of-Flight
LSO	Lutetium Oxyorthosilicate
SiPM	Silicon Photomultiplier
ROI	Region-of-Interest
TAC	Time-Activity-Curve
PVE	Partial-Volume-Effect
VL	Vascular Volume Fraction
PTF	Perfusable Tissue Fraction
DTF	Dead-Time Correction Factor
FBP	Filtere-Back-Projection
OSEM	Ordered-Subset-Expectation-Maximization

PSF	Point-Spread-Function
NEMA	National Electrical Manufacturers Association
APD	Avalanche Photodiode
SUV	Standardized Uptake Value
EARL	European Association of Nuclear Medicine in Research Ltd.
D690	Discovery 690
DMI-20	Discovery MI with four detector rings
Vision-600	Biograph Vision 600
VOI	Volume-of-Interest
ISF	Input Signal Fraction
SD	Standard Deviation
GFS	Gaussian Filter Size
AUC	Area-Under-Curve
SF	Scatter Fraction
LAD	Left Anterior Descending
LCX	Left Circumflex
RCA	Right Coronary Artery

List of Original Publications

This dissertation is based on the following original publications, which are referred to in the text by their Roman numerals:

I **Siekkinen Reetta**, Teuho Jarmo, Smith Nadia A.S., Fenwick Andrew, Kirjavainen Anna K., Koskensalo Kalle, Saraste Antti, Teräs Mika. Study of the Effect of Reconstruction Parameters for Myocardial Perfusion Imaging in PET With a Novel Flow Phantom. *Frontiers in Physics*, 2020; 8:1–10.

II **Siekkinen Reetta**, Kirjavainen Anna K, Koskensalo Kalle, Smith Nadia A.S., Fenwick Andrew, Saunavaara Virva, Tolvanen Tuula, Iida Hidehiro, Saraste Antti, Teräs Mika, Teuho Jarmo. Assessment of a digital and an analog PET/CT system for accurate myocardial perfusion imaging with a flow phantom. *Journal of Nuclear Cardiology*, 2021s; 29:1964–1972.

III **Siekkinen Reetta**, Han Chunlei, Maaniitty Teemu, Teräs Mika, Knuuti Juhani, Saraste Antti, Teuho Jarmo. A retrospective evaluation of Bayesian-penalized likelihood reconstruction for $[^{15}O]H_2O$ myocardial perfusion imaging. *Journal of Nuclear Cardiology*, 2023; 30(4):1602–1612.

IV **Siekkinen Reetta**, Partanen Heidi, Kukola Linda, Tolvanen Tuula, Fenwick Andrew, Smith Nadia A.S., Teräs Mika, Saraste Antti, Teuho Jarmo. Preliminary Protocol for Measurement of Reproducibility and Accuracy of Flow values on Digital PET/CT Systems in $[^{15}O]H_2O$ Myocardial Perfusion Imaging Using a Flow Phantom. *Manuscript.*

1 Introduction

Myocardial perfusion imaging (MPI) using Positron Emission Tomography (PET) allows quantitative measurements of absolute myocardial blood flow (MBF) (Knuuti et al., 2009). MPI with PET is conducted using short-lived tracers, such as $[^{15}O]H_2O$, that allow direct measurements of MBF from dynamic PET images.

In recent years, there have been several developments in PET detector technologies, resulting in the introduction of novel digital PET systems. Digital PET systems have nearly two-fold sensitivity compared to conventional analog-only PET systems, and also their count-rate capabilities have been improved (David F.C. Hsu et al., 2017). Advanced PET count-rate capabilities are beneficial in MPI studies as count-rates during the short MPI acquisition vary from very high to very low. Therefore, more efficient system performance allows more accurate quantification of MBF.

Along with the introduction of digital PET systems, novel image reconstruction techniques are increasingly applied not only in oncological PET imaging but also in MPI. The new commercially introduced reconstruction method, Block Sequential Regularized Expectation Maximization (BSREM), has already shown to offer more accurate lesion detection (Ross, 2014) but only few studies have evaluated its use in MPI.

However, there have been no proper reference standards available, that would allow accurate and reproducible measurements of different methodologies affecting the quantification of MBF. Recently, Gabrani-Juma et al. provided a standard platform for MPI PET validation purposes (Gabrani-Juma et al., 2017). This flow phantom offers an ideal ground truth for investigating the effect of different count-rate measurements, reconstruction parameters, and other technical factors contributing the image-derived flow values. In addition, the flow phantom would allow developing a reproducible harmonization protocol, which would ease the comparison of MBF values within different PET system generations, acquisition facilities and cardiac centres.

This thesis focuses on assessing the PET system performance on MPI, evaluating the novel reconstruction methods and their accuracy on MBF quantification, and developing a preliminary protocol for assessing the reproducibility and accuracy of

digital PET systems on MPI using a novel flow phantom in order to achieve the full potential of digital PET/CT systems as well as diagnostic accuracy in MBF quantification.

2 Review of the Literature

2.1 Myocardial Perfusion Imaging

The concept *perfusion* is defined as "the passage of fluid through the lymphatic system or blood vessels to an organ or a tissue" (Antonini, 2010) and is "the volume of blood flowing through certain mass (or volume) of tissue per unit time" (Oikonen, 2019) and is therefore usually given in units of millilitres of blood per 100 grams of tissue per minute [ml/(100 g * min)] (Oikonen, 2019). *Perfusion imaging* therefore aims at *measuring* (quantitating) the volume of blood flow over time in the selected tissue.

Therefore, MPI aims at quantitating blood flow rate in myocardial tissue, named MBF. MBF is thereafter defined as "the volume of blood transiting through (the myocardial) tissue at a certain rate" (Moccetti and Lindner, 2019) and is also given in units of [ml/(100 g * min)]. MPI is essential when diagnosing cardiovascular diseases, as several cardiovascular diseases may affect MBF and restrict the blood supply into myocardium. The most common cardiovascular disease affecting MBF is obstructive coronary artery disease (CAD). Therefore, MPI is an accurate tool for the classification of myocardial ischemia caused by obstructive CAD (Heinle and Siraj, 2009).

When evaluating MBF, MPI may be conducted during pharmacologically induced vasodilator stress. Vasodilator stress reveals the perfusion defects in myocardium as in stress MBF increases three-fold compared to rest MBF due to increased blood demand in myocardium. Therefore the stenosis in coronary arteries creates a rate limiting factor for MBF and thereafter enhances the limited MBF in contrast to normal MBF in myocardium (Nammas *et al.*, 2021). Thus, the "stress MPI" is a key tool for revealing abnormal myocardial perfusion (Reyes, 2016). However, MPI can also be conducted without stress, as "resting-only" or alternatively, under both stress and rest conditions. Thereafter, one can use information provided under stress and rest myocardial perfusion when preparing the myocardial ischemia interpretation. What is more, myocardial flow reserve (MFR) reveals the relative reserve of coronary circulation as it is the relative measure of stress MBF compared to rest MBF (Ziadi, 2017) and it can be used for diagnosing

the myocardial ischemia, as it corresponds to the ratio of stress to rest myocardial perfusion (Danad *et al.*, 2014).

MPI can be conducted with several medical imaging modalities, such as Computed Tomography (CT), Single Photon Emission Computerized Tomography (SPECT), or Magnetic Resonance Imaging (MRI). PET MPI however allows non-invasive quantification of MBF (Knuuti *et al.*, 2009). The European Association of Nuclear Medicine (EANM) has recently published procedural guidelines for the diagnosis and management of chronic coronary syndromes (Sciagrà *et al.*, 2021). The guidelines suggest using PET MPI as the first line diagnostic test in patients with suspected obstructive CAD.

2.2 MPI with Positron Emission Tomography

PET

PET uses radioactive positron emitting tracers injected into the circulation of a subject. The tracer radioactivity decays with β^+ decay, and when the emitted positron interacts with an electron within a subject's tissue, annihilation occurs and two 511 keV photons are emitted into opposing directions. Thereafter, PET detects the opposing photons with opposing detectors. The opposing photons therefore form a coincidence event and a line-of-response (LOR). The number of photons detected are referred to as counts that include true coincidence events, scattered events, and random events. (Bailey *et al.*, 2014)

MPI Tracers

Usually, MPI PET applies short-lived tracers, such as $[^{15}O]H_2O$, which has a half time of 124 s (Lederer, Hollander and Perlman, 1967; Knaapen and Lubberink, 2008). Other tracers used are $[^{82}Rb]$ with a half time of 76 s (Lederer, Hollander and Perlman, 1967; Germino *et al.*, 2016) and $[^{13}N]NH_3$ with a half time of 9.96 min (Lederer, Hollander and Perlman, 1967; Fiechter *et al.*, 2012). The advantage of $[^{15}O]H_2O$ compared to other tracers is that it is freely diffusible and inert and therefore the activity uptake in myocardial tissue corresponds perfusion linearly up to the highest MBF values (Knuuti *et al.*, 2009). $[^{15}O]$ is produced in a cyclotron and finally $[^{15}O]H_2O$ is automatically injected in the subject via bolus delivery system (Kajander *et al.*, 2010).

Dynamic MPI PET Acquisition

MPI PET is acquired as dynamic acquisition meaning that the whole acquisition is divided into certain number of time frames. Dynamic acquisition allows following the tracer passage from the heart circulation to coronary arteries and myocardial tissue.

PET detects the highest number of counts at the beginning of the MPI acquisition when the tracer is present in the heart circulation, and especially in the left ventricle. After that, the count-rates start decreasing, as the tracer activity decays and the tracer passes into the subject's systemic circulation. Therefore, there is a clear difference in count-rates at the beginning compared to the end of the MPI PET acquisition.

The count-rates are divided into four groups: total prompts (=counts) (P), trues (T), randoms (R), and scatter (S) (Bailey *et al.*, 2005). The true counts are defined as follows

$$T = P - S - R \tag{1}$$

(Grant *et al.*, 2016). Therefore, the higher the activity level present within a time frame, the higher the number of total counts (prompts). The count-rate performance of a PET system can be investigated in terms of noise-equivalent count-rates (NECR). NECR is "that count rate which would have resulted in the same signal-to-noise ratio (SNR) in the data in the absence of scatter and random events" (Bailey *et al.*, 2005). Therefore, NECR offers a possibility to compare the count-rate performance between systems. When activity in the field-of-view (FOV) of the system increases, the number of random events is proportional to activity squared because coincidence detection happens in detector pairs. This behaviour is presented in the publication by Bailey *et al*. where a schematic NECR curve (Figure 3.19 on page 55 in chapter 3) shows that with high activity the amount of random events exceeds the number of true events and random events' relative contribution to image quality is higher (Bailey *et al.*, 2005). As the number of true counts is the key factor determining the PET image accuracy, it is essential to maintain at the optimal count-rate level during the entire MPI PET acquisition.

Similarly, the PET system detector dead-time is higher at the beginning due to pulse pile-up (Bailey *et al.*, 2005) compared to the end of the MPI PET acquisition. Dead-time is defined as the time when the detector is not capable of receiving new events due to the processing time of the previous detected event (Bailey *et al.*, 2005). Therefore, it is essential to ensure that the detector dead-time also stays on optimal level during the entire acquisition. Otherwise, the detector dead-time may limit the number of collected prompts and that may affect negatively on PET image quality and the accuracy of MBF quantification. What is important, the number of true

counts and the level of PET detector dead-time are dependent on the PET system count-rate performance.

From Analog to Digital

The conventional PET systems are so called "analog-only" systems, which were frequently used until the introduction of digital PET systems. The detector technology in analog PET systems was large, bulky, and slow, which rose the need for more advanced PET detector technique that could offer more efficient count-rate performance capabilities with higher spatial resolution and timing resolution.

The detectors in the analog PET systems were based on photomultiplier tubes (PMTs) and the size of their detecting area was approximately 10 times larger than nowadays with the digital PET systems (Bailey *et al.*, 2014). Also, the analog PET systems used similar weighted location algorithms for photon location estimation, as the Anger-logic gamma cameras. Therefore, that compromised their spatial resolution (Bailey *et al.*, 2014). In the novel digital PET system such algorithms are not necessarily needed. What is more, PMTs do not directly convert the light emitted from the scintillator photons to electric current, compromising the detector's timing resolution (Germano, Berman and Slomka, 2016).

The very first commercial analog PET systems also used principally bismuth germanate (BGO) -based scintillators, which are powerful converting the 511 keV photons to light photons but have poor intrinsic timing resolution (Cherry, Sorenson and Phelps, 2012). Therefore, they were not entirely optimal for fast detection, which is needed for example for estimating the time-of-flight (TOF) of the two opposing 511 keV photons. TOF uses the photon's time-of-arrival information at the detector, calculates the time difference between detected coincidence photons, and enables calculating the annihilation location at the LOR (Vandenberghe *et al.*, 2016). There was therefore a need for more efficient scintillators, and the most common ones nowadays used are the lutetium-based crystals, such as lutetium oxyorthosilicate (LSO) (Bettinardi *et al.*, 2011). The lutetium-based scintillators have faster intrinsic timing characteristics, making it also highly suitable for dynamic PET studies, such as for MPI.

In recent years, several vendors have developed and commercialized so-called "digital" PET systems. The need for such PET systems was partly due to the fact that PMTs are not properly functioning in magnetic field, affecting the development of advanced PET/ MRI systems. Therefore, the digital systems nowadays commonly use silicon photomultipliers (SiPMs) (Lecoq and Gundacker, 2021) with lutetium-based scintillators (Globus and Grinyov, 2006). SiPMs convert the light photon from the scintillator directly to electric current making them less susceptible for magnetic field. Also, the surface of the SiPMs is divided into several microcells, each of which

is capable of receiving the photon and passing it forward for the electrical circuit (Vandendriessche *et al.*, 2019). The electrical circuit thereafter processes the photons, and collects the photon energy, time stamp, and location (GE Healthcare, 2017). SiPMs can save more photons, with more accurate locations and time stamps, compared to PMTs. The digital PET detectors based on SiPMs and lutetium-based crystals are rapid, provide higher spatial resolution, sensitivity, and peak NECR compared to the analog-only PET systems (Bettinardi *et al.*, 2011; Hsu *et al.*, 2017). As a result, the digital PET/CT systems offer several advantages over the analog systems. Recently, several digital systems have now come to the market and offer a faster option for photon detection (Sciagrà *et al.*, 2021).

2.3 Quantitative MPI

MBF quantification allows extracting MBF values in absolute units of millilitres per gram of myocardial tissue per unit time [ml/g/min] from dynamic PET images. To derive quantitative MBF values it is first essential to formulate a mathematical kinetic model equations that describe the tracer characteristics and represent the measured measured tracer kinetics well. There are several kinetic models developed for each tracer specifically (Morris *et al.*, 2004).

MBF quantification is started by determining the activity concentration in the left ventricle (blood pool) as well as in the myocardial tissue within each time frame for the entire dynamic PET MPI acquisition based on regions-of-interests (ROI). This results into deriving time-activity curves (TACs) that express the tracer concentration in left ventricle and myocardium as a function of time in units of MBq/ml. The kinetic model parameters are determined so that the modelled curves reproduce the measured left ventricle and myocardial TACs well enough (Iida *et al.*, 1988). Kinetic modelling is performed for all pixels within the myocardial ROI. The output of the process is a parametric image that expresses MBF for each image voxel in the myocardial ROI. The parametric image is arranged as the standard MBF polar map for clinical interpretation. There are several software that provide semi-automatic tools for defining ROIs, extracting the TACs, showing MBF values as well as visualizing the results in a standard polar plot (Harms *et al.*, 2014).

$[^{15}O]H_2O$ Modelling

When it comes to quantification of MBF from $[^{15}O]H_2O$ dynamic MPI PET images, there is a specific model for $[^{15}O]H_2O$ MBF quantification developed by Iida *et al.* (Iida *et al.*, 1988, 1991, 1992). The model is in clinical use in Turku PET Centre. $[^{15}O]H_2O$ flow modelling is based on a two-compartment (one-tissue compartment) model (Iida *et al.*, 1988).

The two-compartmental kinetic model includes two rate constants, K1 and k2, the first expressing the rate of tracer that transfers from blood to the myocardial tissue, and the second expressing the rate of tracer that goes back from the myocardial tissue to blood stream (Figure 1) (Walter, 1986; Oikonen, 2019). The rate of tracer change in tissue over time (dC1(t)) can be expressed as follows

$$dC1(t)/d(t) = K1 \cdot Cb(t) - k2 \cdot C1(t), \quad (2)$$

where Cb is the tracer activity concentration in arterial blood. C1(t) can be solved as follows

$$C1(t) = K1 \cdot Cb(t) * e^{-k2 \cdot t}, \quad (3)$$

where $*$ is the convolutional operator. However, as the myocardial TAC (R(t)) is derived from PET images and used as C1(t) in kinetic modelling, it contains 1) error from heart movement (Iida *et al.*, 1988), 2) error from the limited spatial resolution of PET i.e. partial-volume-effect (PVE) (Iida *et al.*, 1988), and 3) error from activity spill-over from the left ventricle as well as fraction from the arterial blood-volume (Iida *et al.*, 1991). Therefore, R(t) becomes as follows (Iida *et al.*, 1991)

$$R(t) = f \cdot \alpha \cdot Cb(t) * e^{-k2 \cdot t} + VL \cdot Cb(t), \quad (4)$$

where *f* is the regional blood flow in units of [ml/min/g] and α is the ratio of the tissue mass to the volume of the region of interest in units of [g/ml], and *VL* is the factor that contributes for the spill over and fractional arterial blood-volume (the vascular volume fraction) (Iida *et al.*, 1991). α is defined as follows

$$\alpha = W/V, \quad (5)$$

where *W* corresponds to the tissue mass in units of [g] and *V* the volume of the ROI in units of [ml] (Iida *et al.*, 1988). Therefore, α corrects for the underestimation of myocardial radioactivity due to PVE (Iida *et al.*, 1991). Without α, the resulting MBF would suffer from PVE (Iida *et al.*, 1988). Therefore, K1 now corresponds to

$$K_1 = f \cdot \alpha, \quad (6)$$

In addition, k2 can be expressed as

$$k_2 = f/p, \quad (7)$$

where p is the partition coefficient, which in this case is the "ratio of the water content in the myocardium to that in the blood" (Iida *et al.*, 1988). This model assumes that p can be fixed, and is 0.91 ml/g (Iida *et al.*, 1988).

What is more, the image-derived left-ventricular time-activity curve (LV(t)) should also be corrected for spill-over from the myocardial tissue as well as for PVE as LV(t) is used as Cb(t) (Iida *et al.*, 1992). Therefore LV(t) is expressed as

$$LV(t) = \beta \cdot Cb(t) + \gamma \cdot \rho \cdot C1(t), \tag{8}$$

where β corresponds to the activity recovery coefficient of the left ventricular ROI, γ the spill-over fraction from the myocardial tissue, and ρ the myocardial tissue density in units of [g/ml]. The Equations 6 and 7 are fitted to the left-ventricular and myocardial TACs and MBF, α (later in this thesis named as the perfusable tissue fraction, PTF), and VL are derived. (Iida *et al.*, 1991) PTF plays a role in the differentiation of viable myocardium from infarct scar (Grönman et al., 2021). This model eventually allows defining larger and smoother ROIs for the left ventricle as the LV(t) is corrected for spill-over from myocardial tissue (Iida *et al.*, 1992). The TACs are corrected for radioactive decay (Iida *et al.*, 1991, 1992).

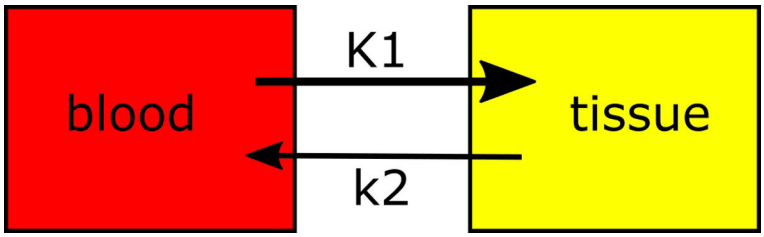

Figure 1. Two-compartmental model accounts for deriving parameters K_1 and k_2.

2.4 Reference Standard Objects for MPI

In medical imaging, reference standard objects, namely phantoms, are used for performance assessment and calibration. The phantoms provide ground truth values for medical images and are therefore essential when user wants to validate the accuracy of different systems. For example, the true, measured, and calibrated activity concentration inside a phantom can be compared against the activity concentration values extracted from PET images. Thereafter, that information can be used for PET system calibration purposes.

Quality control and technical standardization in PET is essential as there are several factors that affect PET quantification (Boellaard, 2009). Typically in PET imaging, the phantoms applied in quality control purposes are so-called "static"

phantoms (Mawlawi *et al.*, 2019) in which activity concentration only decays over time but no other kinetics are examined. However, in MPI PET it is essential that the tracer kinetics are considered when using phantoms for technical standardization purposes. Therefore, MPI PET requires phantoms that simulate myocardial perfusion and allow extracting quantitative values that correspond MBF.

There are some options available for such phantoms, such as a perfusion phantom developed by Chiribiri *et al*. They validated the phantom for magnetic resonance perfusion imaging (Chiribiri *et al.*, 2013), but also used it in PET-MRI (O' Doherty *et al.*, 2017). Similar flow phantom that simulates MBF has been presented by Gabrani-Juma *et al*. and it has been validated for both PET and Single Photon Emission Computerized Tomography (SPECT), and is compatible for both Computed Tomography (CT) and MRI (Gabrani-Juma *et al.*, 2017). Such phantoms have been mainly used for research purposes but allow technical observation of different factors that may influence MBF quantification. The modelled flow phantom parameters mimic the K_1 and k_2 rate parameters and therefore the flow phantoms offer a ground truth for the clinical MBF values (Gabrani-Juma *et al.*, 2017).

2.5 Image Reconstruction in MPI

PET Image Reconstruction

PET systems can acquire data in list-mode or sinogram format. List-mode data contains information of each count detected by each detector element and is saved with the detection time stamp, photon energy, and location information. In addition, TOF (Vandenberghe *et al.*, 2016) information of the counts is saved into the list-mode data.

In the reconstruction process, the list-mode data is usually first binned (histogrammed) into sinograms. In sinograms "variables s and Φ define the location and orientation of the LOR" (Bailey *et al.*, 2005) for all counts. Thereafter, the reconstruction process involves a mathematical algorithm that provides an image estimate from the sinogram data.

However, the data needs multiple corrections to allow accurate quantification of the PET images. These include such as: correction for scattered events (Ollinger, 1996; Watson, Newport and Casey, 1996), random events (Stearns *et al.*, 2004), detector dead-time (Lewellen *et al.*, 1994), and photon attenuation (Reader and Zaidi, 2007). For attenuation correction purposes and anatomical localization, CT is the current standard (Koepfli *et al.*, 2004). Dead-time correction gives a dead-time correction factor (*DTF*), which is based on the detector live-time data in order to calculate the detector pile-up losses (Lewellen *et al.*, 1994).

There are several mathematical algorithms that have been developed for PET image reconstruction. Nowadays, the PET reconstruction algorithms are based on statistical, iterative reconstruction methods. In general, iterative reconstructions provide better SNR compared to previous analytical algorithms, such as Filtered Back Projection (FBP) (Shi *et al.*, 2018). The most used iterative reconstruction is Ordered Subset Expectation Maximization (OSEM) reconstruction (Tong, Alessio and Kinahan, 2010). In OSEM reconstruction, the number of iterations and subsets defines the final convergence rate of an image.

However, recently, novel reconstruction methods have been under investigations and have thereafter become available in commercial PET systems. One of such reconstruction method is BSREM algorithm (Caribé *et al.*, 2019) (vendor name Q.Clear from GE Healthcare). In comparison to OSEM, BSREM reaches full convergence whereas OSEM iterates up to a predetermined number of iterations and subsets that cannot be increased to infinity due to increase in image noise (Ross, 2014). In order to control noise, BSREM incorporates an additional term, a penalty parameter β in the iterative process (Ross, 2014). Therefore, BSREM results in several benefits, such as higher image contrast and lower noise when compared to OSEM (Trägårdh *et al.*, 2019).

However, despite much research has been performed in assessing BSREM for oncological imaging, only a few assessments have been made in MPI PET. O'Doherty *et al*. investigated BSREM in $[^{13}N]NH_3$ MPI showing minimal effect in MBF quantification with BSREM (O'Doherty *et al.*, 2017). In addition, Nordström *et al*. showed that BSREM-based diagnosis is comparable to OSEM-based diagnoses with $[^{15}O]H_2O$ on 20 subjects (Nordström *et al.*, 2022). BSREM has also been shown to be applicable for $[^{82}Rb]$ MPI (Christensen and Tolbod, 2017).

When it comes to image reconstruction, there are several other parameters in addition to the reconstruction algorithms that influence the final reconstructed image. One such metric parameter is point spread function (PSF) that models the pixel bias in reconstructed image due to PVE (Bailey *et al.*, 2005). PVE is a consequence of the limited system intrinsic spatial resolution arising from the detector characteristics that also depends on the reconstructed resolution of PET image (Bailey *et al.*, 2005). In image reconstruction, system PSF information can be modelled to account for the positioning accuracy of the detectors (Rahmim, Qi and Sossi, 2013). PSF modelling thereafter increases the image SNR. Including PSF in cardiac PET reconstruction increases image quality (Matheoud *et al.*, 2017). In addition, image matrix size affects the target-to-background (TBR) ratio. Higher matrix size has been showed to improve lesion detectability (Riegler *et al.*, 2017). Therefore, these are the first parameters to be investigated when evaluating the effect of reconstruction parameters on the accuracy on MBF quantification.

Reconstruction in MPI

As already stated in Section 2.3, the count statistics differ throughout the MPI PET acquisition. That causes the image noise to alter throughout the acquisition. In addition, the frame times of the acquisition are shorter in the beginning of the acquisition and increase towards the end of the acquisition. Shorter frame times at the beginning of the scan allow higher sampling of the tracer arrival to left ventricle blood pool. On that account, additional variation in count-rates and image noise occurs within the MPI acquisition. On that account, iterative reconstructions are beneficial for MPI PET that creates images with relatively stable SNR (Moody *et al.*, 2015). Consequently, it is essential that image reconstruction method is optimally selected and validated for MPI PET, in order to guarantee accurate MBF quantification.

Recently, OSEM has been investigated in several cardiac studies (Presotto *et al.*, 2015; Kero *et al.*, 2017; Matheoud *et al.*, 2017; Nordström *et al.*, 2022). Static cardiac imaging with [^{18}F]FDG using OSEM including TOF and PSF (OSEM-TOF-PSF) has been evaluated in studies incorporating static phantoms (Presotto *et al.*, 2015; Matheoud *et al.*, 2017). One focused on evaluating the OSEM-TOF-PSF effect on the defect contrast recovery (Matheoud *et al.*, 2017) and the other on simulating the bolus passage and steady uptake in a cardiac perfusion acquisition (Presotto *et al.*, 2015). The mutual conclusion of the studies was that OSEM-TOF-PSF improves image quality in cardiac PET studies.

However, in MPI PET it is essential that also the dynamic nature of the acquisition is considered. It has been shown that OSEM with or without TOF has no clear effect on quantitative MBF values acquired in clinical [^{15}O]H_2O studies (Kero *et al.*, 2017; Nordström *et al.*, 2022). In addition, the novel BSREM reconstruction has been evaluated for clinical perfusion studies with [^{13}N]NH_3 (O'Doherty *et al.*, 2017). That study showed that MBF was only minimally affected by the novel reconstruction method. A similar conclusion was reported with MPI study using [^{15}O]H_2O (Nordström *et al.*, 2022), in which MBF quantification was investigated in 20 patients.

In general, the recent studies have been able to show that iterative reconstruction improves image quality, but the novel reconstruction methods have no clear effect on MBF quantification in oncological studies or using [^{13}N]NH_3, [^{15}O]H_2O, and [^{82}Rb]. However, the effect of reconstruction parameters must be confirmed with a reference standard, a flow phantom, in which simulation of dynamic acquisition conditions is possible. In addition, the reconstruction effect on clinical interpretation and classification of ischemia should be confirmed.

2.6 System Performance in MPI

Assessment of the physical performance of PET system is a key issue in achieving accurate and reproducible quantitative values in MPI. The count rates are the highest in the left ventricle blood pool during the tracer first pass after injection but depend also on the tracer distribution in the system's FOV during the acquisition. It may be optimal to define an optimal injected dose for each PET system to maintain the count-rates and system dead-time at the system's optimal count-rate and dead-time performance during the entire image acquisition. Otherwise, the TACs may be compromised, and MBF quantification may be inaccurate.

Clinical MPI studies use different tracers, and the injected dose alters across each tracer used. For example, for [^{82}Rb] the European and North American guidelines recommend using 1100-1500 MBq injected activity. In Turku PET Centre the clinical dose for [^{15}O]H_2O is 500 MBq. Walker et al. have proposed optimizing the injected dose by investigating patient-specific noise-equivalent counts (Walker *et al.*, 2009). This method allows measuring the statistical quality in each time frame of dynamic PET (Walker *et al.*, 2009). Lassen et al. investigated that the injected dose may be assessed by comparing full and half dose protocols (Lassen *et al.*, 2020). They showed that with less injected dose, system count-rate performance maintains at optimal level and does not overestimate the MBF values (Lassen *et al.*, 2020). As already stated in Section 2.3, digital PET systems offer potential capabilities for accurate MPI due to their increased sensitivity and peak NECR. Therefore, studying flow quantification accuracy over the count-rates and activities present during the MPI acquisition is the primary requirement when demonstrating the feasibility of digital PET systems for MPI.

The improved count-rate capabilities of digital PET systems have already been shown with National Electrical Manufacturers Association (NEMA) tests (National Electrical Manufacturers Association, 2012; Hsu *et al.*, 2017). In those studies, standard NEMA phantoms and protocols were used. However, static high count-rate phantoms have also been used for investigating dynamic ranges of PET systems (deKemp *et al.*, 2008; Renaud *et al.*, 2017). deKemp *et al*. first proposed a method investigating the high count-rate performance of PET for MPI for an analog system (deKemp *et al.*, 2008). Similarly, Renaud *et al*. investigated the dynamic ranges of several PET systems using [^{82}Rb] (Renaud *et al.*, 2017). They defined the peak prompts, peak singles and peak *DTF* for 11 systems with different detector techniques and system sensitivities. The peak values were used to define the maximum injected activity per patient mass during the bolus first-pass. The highest peak prompts and, also the highest *DTF* were measured with the Discovery IQ (GE Healthcare, Milwaukee, US) (Reynés-Llompart *et al.*, 2017) system. The IQ system uses BGO scintillators and PMTs but has 26 cm axial FOV, which increases the

sensitivity of the system. In comparison to system using lutetium-based scintillators, lower *DTF* was measured with Discovery 690 with peak prompts of 5.9 Mcps. Their study was published before the introduction of commercial digital systems and therefore no such systems were investigated. However, van Dijk *et al*. used static phantoms for investigating the digital PET system high count-rate capabilities (van Dijk *et al.*, 2019). Superior performance was measured with the digital system, and the maximal measured activity was comparable to the analog counterpart. In addition, *DTF* was lower for the digital system, as expected.

However, it is of paramount importance to take not only the high-count rate environment but also the dynamic conditions of MPI into account. O'Doherty *et al*. applied a cardiac perfusion phantom in their high count-rate studies for PET/MRI system that contains avalanche photodiodes (APDs), the prior version of the SiPMs (O' Doherty *et al.*, 2017). They were able to extract TACs from those parts of the phantom that mimic aorta and myocardium and the study indicated that above a certain limit, the quantitative perfusion values are affected by the count-rate losses. However, they studied no *DTFs*, scatter or randoms, even though the role of those parameters is essential in high count-rate studies. As the phantom presented by Gabrani-Juma *et al*. (Gabrani-Juma *et al.*, 2017) was validated for PET and offers advantages for defining both the count-rate performance as well as the flow quantification accuracy over various injected activities for the digital PET system, it could be used to investigate and define optimal counting rate conditions for MPI studies as well.

2.7 System Technical Standardization in MPI

It is commonly recognized that both physical and methodological factors may negatively alter the quantitative PET values across patients and systems. Boellaard *et al*. have presented a large review of factors affecting the quantification in PET, focusing on standardized uptake value (SUV) quantification (Boellaard, 2009). Several guidelines have addressed the PET quantification and harmonization issues in [^{18}F]FDG oncology imaging (Boellaard, 2009). As a result, EANM and the European Association of Nuclear Medicine in Research Ltd. (EARL) have published an accreditation program which is intended for harmonizing SUV values in [^{18}F]FDG tumour assessment, across different PET systems from several generations as well as across PET centres. In a nutshell, they have proposed that the PET system harmonization procedure should be conducted using NEMA phantoms and implementing similar technical calibration practices as well as quality control protocols across all PET centres. Thereafter, it is possible to perform multicentre trials in oncology imaging using [^{18}F]FDG, despite of which PET system is used in

each centre. However, whenever new radionuclides are proposed for clinical use, there is a need for an update of the harmonization instructions (Aide *et al.*, 2017).

When it comes to MPI, it is also of high importance to address harmonization issues arising from different PET system performances as well as from the uncertainty factors affecting the MBF quantification. In very recent discussion, Moody *et al*. stated that there is a growing need for technical standardization regarding not only oncology imaging but also MPI PET (Moody, Ficaro and Murthy, 2020). However, only a few studies have investigated that issue due to the fact that no validated standard platforms have been commercially available before. With a standard platform, similar calibration protocols as published by EARL and EANM could be developed for MPI and thereafter MBF quantification as well (Gabrani-Juma *et al.*, 2017). Thereafter, standardization in MBF values across all cardiac PET centers and different PET/CT systems should become a clinical routine. In conclusion, the harmonization procedures across PET systems from multiple vendors could be established by unifying study procedures, reconstruction parameters, counting-rate conditions as well as injection protocols (Aide *et al.*, 2017).

3 Aims

To assess the capabilities and advantages of digital PET/CT system for MPI by:

1. Defining the effect of different PET reconstruction techniques for [^{15}O]H_2O myocardial perfusion imaging.
2. Assessing flow quantification accuracy of a novel digital PET/CT system in comparison to an analog PET/CT system.
3. Evaluating BSREM reconstruction for quantification of MBF in patients with suspected coronary artery disease.
4. Evaluating the contribution of different technical factors on the accuracy and reproducibility of MBF values using a preliminary measurement protocol.

4 Materials and Methods

4.1 Performance Characteristics of PET Systems

Table I shows the performance characteristics of the PET systems, Discovery 690 (D690, GE Healthcare, Milwaukee, US, release year 2009), Discovery MI with four detector rings (DMI-20, GE Healthcare, Milwaukee, US, release year 2016), and Biograph Vision 600 (Vision-600, Siemens Healthineers, Erlangen, Germany, release year 2018), that were used in this thesis.

Table 1. Performance characteristics of PET systems Discovery 690 (D690, GE Healthcare, Milwaukee, US), Discovery MI (DMI-20, GE Healthcare, Milwaukee, US), and Biograph Vision 600 (Vision-600, Siemens Healthineers, Erlangen, Germany) used in the studies. The characteristics are based on the NEMA publications by Bettinardi *et al*., Hsu *et al*., Van Sluis *et al*., and Reddin *et al*. (Bettinardi *et al.*, 2011; Hsu *et al.*, 2017; Reddin *et al.*, 2018; Van Sluis *et al.*, 2019). Modified from original publications I and IV.

	Unit	**D690**	**DMI-20**	**Vision-600**
Number of Detector Rings		24	4	8
Transaxial FOV	cm	70	70	78
Axial FOV	cm	15.7	20	26.1
Crystal Material	-	LYSO	LSO	LSO
Crystal Array	-	9 x 6	4 x 9	5 x 5
Crystal Size	mm × mm × mm	4.2 × 6.3 × 25.0	3.95 × 5.3 × 25.0	3.2 × 3.2 × 20.0
Detector Type	-	Square PMT	SiPM	SiPM
Sensitivity	cps/kBq	7.4	13.7	16.4
Spatial Resolution	rad @ 1 cm	4.7	4.1	3.5
Peak NECR	kcps	139	193	306
Peak NECR Activity	kBq/ml	29	21.9	32
Peak NECR Scatter Fraction	%	37	40.6	38.7
Timing Resolution	ps	544	375	210
Energy Resolution	%	12.4	9.4	9.0

4.2 Flow Phantom

The studies I, II, and IV used a flow phantom for data measurements.

4.2.1 Construction

The flow phantom (Figure 2, Figure 3) is described in the publication by Gabrani-Juma *et al*. in which a detailed photograph of the phantom can be seen (Gabrani-Juma *et al.*, 2017) (Shelley Medical Imaging Technologies, Ontario, Canada). The phantom simulates myocardial perfusion and allows to quantitate flow values that correspond to MBF.

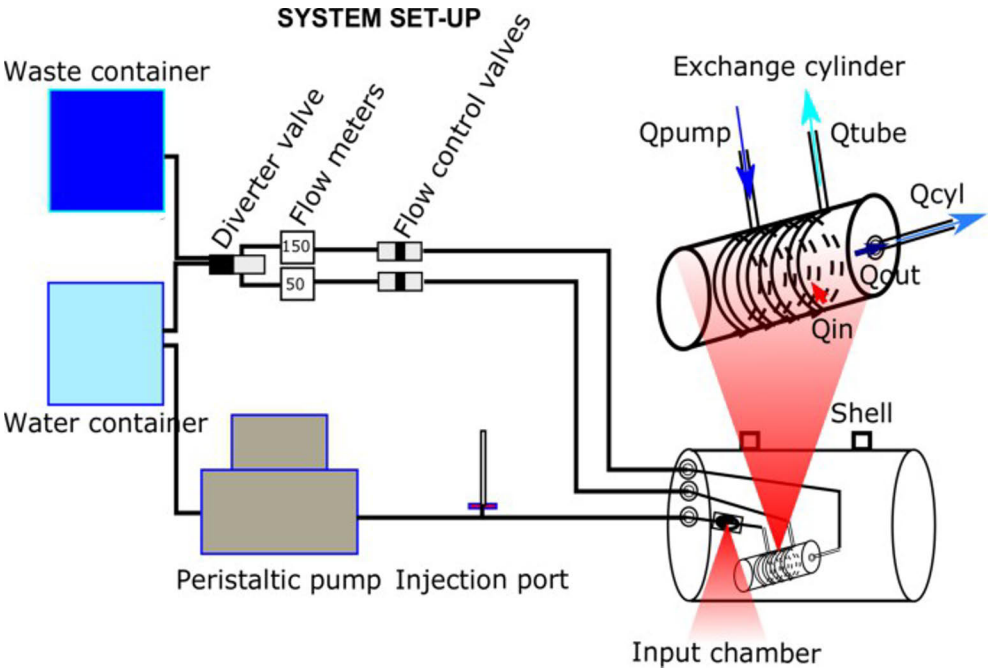

Figure 2. Flow phantom system illustration (not in scale).

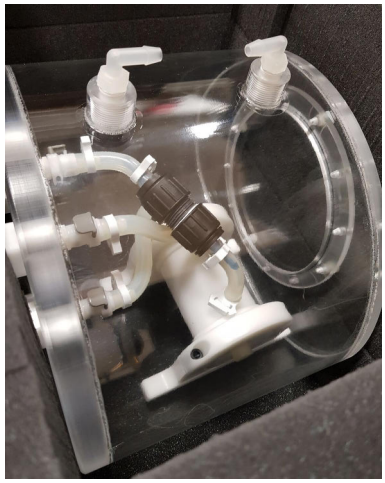

Figure 3. Image of the flow phantom's shell that contains the input chamber and exchange cylinder.

The flow phantom consists of several compartments that are connected with hoses. A peristaltic pump manages water flow within the system and takes water into the system from an external water container. The flow value managed by the pump is named Qpump. The flow phantom system also includes another container that works as a waste-water container. It collects water that has run through the phantom system. However, it is possible to run the phantom by closed or open looped, meaning that recirculation of water is possible within the phantom. A diverter valve determines whether the water circulates back to the first water container.

After the peristaltic pump the system comprises a dose injector port, that is connected to the [^{15}O]H_2O delivery system. The injector port is connected through a hose to the input chamber of the phantom, which mimics the left ventricle blood pool. The input chamber (volume of 15.7 ml) is connected to an exchange cylinder inside which there is a perforated tube. That compartment simulates the myocardium. Ten holes in pairs allow the water to permeate from the perforated tube into the volume of the exchange cylinder, simulating the perfusion within the myocardial tissue. The input chamber and the exchange cylinder are surrounded by a water shell which has similar dimensions as the NEMA image quality phantom. The water shell mimics the soft tissue of a human body and simulates body scatter and attenuation.

The perforated tube and the exchange cylinder have their own hoses that are connected to flow control valves as well as to flow meters, each having their own. The flow control valves allow constricting the flow within the perforated tube as well as in the exchange cylinder as preferred by the user in order to mimic different flow rates in myocardium. The flow measured from the perforated tube is namely Qtube

and flow from the exchange cylinder is namely Qcyl. Ideally, the pump flow should be equal to the flow in the perforated tube and exchange cylinder

$$Q_{pump} = Q_{tube} + Q_{cyl}. \quad (9)$$

Finally, Qcyl value is converted to reference flow value (Qref) when the exchange cylinder flow meter calibration value is multiplied by Qcyl. The calibration value is extracted from a look-up table and is based on the flow meter calibration protocol as suggested by the vendor.

4.2.2 Kinetic Modelling

The phantom incorporates a two-compartmental model that is specifically designed for the phantom (Gabrani-Juma *et al.*, 2017) (Figure 4). First, the model requires defining the volumes-of-interests (VOIs) as a function of time for the input cylinder ($C_{inputVOI}$(t)) and exchange cylinder (C_{cylVOI}(t)). Thereafter, the activity concentration within the perforated tube as a function of time (C_{tube}(t)) is estimated by using a transport delay factor *delay* and $C_{inputVOI}$(t) as follows

$$C_{tube}(t) = C_{inputVOI}(t - delay). \quad (10)$$

Thereafter, the two-compartmental model equation for the activity concentration inside the exchange cylinder can be defined as follows:

$$C_{cyl}(t) = q_{in}e^{-q_{out}t} * C_{tube}(t), \quad (11)$$

where $*$ marks the convolution operation. The rate constant parameters q_{in} and q_{out} correspond for K_1 and k_2 rates and are analogous to the wash-in and wash-out rates to and from the myocardium with units of min^{-1}. The rate constants are converted to flow values by multiplying q_{in} and q_{out} with the total volume of the exchange cylinder V_{cyl} (160 ml). Therefore, the flow out from the perforated tube to the exterior volume of the exchange cylinder is Qin and the flow out from the exchange cylinder is Qout. Ideally,

$$Q_{ref} = Q_{in} = Q_{out}. \quad (12)$$

As the VOI covering the exchange cylinder contains contributions from both C_{cyl}(t) and C_{tube}(t), it is corrected for signal mixing as follows:

$$C_{cylVOI}(t) = ISF \cdot C_{tube}(t) + (1 - ISF) \cdot C_{cyl}(t), \quad (13)$$

where *ISF* is the input signal fraction. The final model consists of four free modelling parameters: q_{in}, q_{out}, *ISF* and *delay*. (Gabrani-Juma *et al.*, 2017)

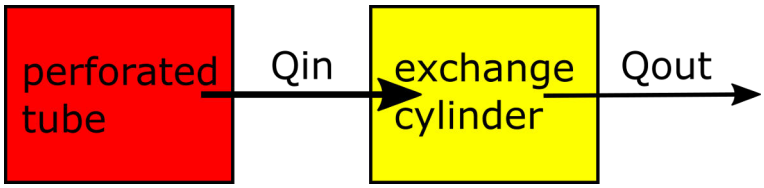

Figure 4. The compartmental model diagram for the flow phantom.

4.2.3 QuantifyDCE

The flow phantom data analysis is run with the vendor-provided software Quantify DCE 1.1 (Shelley Medical Imaging Technologies, Ontario, Canada).

First, the input chamber as well as the exchange cylinder VOIs are defined semi-automatically within the software. The user defines the location for the input chamber and exchange cylinder around which the software defines a fixed size sphere. The sphere radius is 4 cm for the input chamber and 6 cm for the exchange cylinder. Thereafter, VOI is determined based on fixed threshold parameters. Activity concentration values within 15% from the maximal activity concentration inside the sphere form the VOI. The pixel size is 19 mm^3.

Thereafter, the software automatically extracts the input and exchange cylinder (=tissue) as well as performs the model fitting, outputting the modelled TACs of which it determines the rate parameters and eventually Qin and Qut values. Finally, all modelling parameters and flow values are shown in report.

4.3 Effect of Reconstruction Parameters on MPI (I)

This study included the DMI-20 system as well as the flow phantom (details in Sections 4.1 and 4.2).

4.3.1 Data Acquisition

Data acquisition followed the clinical protocol used in Turku PET Centre (Maaniitty *et al.*, 2017). Acquisitions were repeated five times in the same order to ensure the repeatability of the flow values. Qpump was set to 200 ml/min, and Qcyl was constricted to 60% of Qpump. Thereafter, Qcyl values for the five acquisitions were approximately 120 ml/min (mean ± standard deviation (SD) = 121 ml/min ± 1.2 ml/min) and Qtube values were approximately 98 ml/ min (mean ± SD = 97.8 ml/min ± 0.4 ml/min).

At the start of the measurement, the flow meters, peristaltic pump (MasterFlex L/S, 07522-20, US) and [^{15}O]H_2O dispenser (Hidex Oy, Finland) were calibrated. First, a CT scan was acquired for the five acquisitions individually for attenuation correction purposes. Tube voltage was 120 kVp with 63-64 mAs.

The flow phantom was set in the center of the PET FOV. Thereafter, the targeted injected activity was set to 500 MBq by the automatic [^{15}O]H_2O bolus delivery system. The actual administered bolus activities were (mean ± SD) 485 MBq ± 12.7 MBq across the five acquisitions. In the first four tests, the PET scan was started 50 seconds after the dose injection, and in the last test, 51 seconds scan start delay was applied. PET acquisition lasted 4 minutes and 40 seconds, and the data was binned into 24 time frames of 14 × 5 s, 3 × 10 s, 3 × 20 s and 4 × 30 s, following the clinical protocol (Kajander *et al.*, 2010).

4.3.2 Reconstructions

In order to evaluate the effect of different reconstruction parameters on the quantitative accuracy of MPI, several reconstructions were applied. All reconstructions included corrections for scatter, randoms, dead-time, attenuation, geometry, etc. In all OSEM reconstructions, three iterations with 16 subsets were used. The reconstructed FOV size was 50 cm in all reconstructions.

First, data was reconstructed using OSEM with or without TOF as well as PSF with a fixed Gaussian filter size (GFS) and matrix size. GFS was 5 mm and matrix size 192 × 192. These reconstructions were namely: OSEM, OSEM-TOF, OSEM-PSF, and OSEM-TOF-PSF.

Second, data was reconstructed using OSEM-TOF-PSF with three other matrix sizes: 128 × 128, 256 × 256, and 384 × 384.

Third, data was reconstructed using OSEM-TOF-PSF with two other GFSs: 4 mm and 8 mm.

Finally, data was reconstructed using BSREM (vendor name Q.Clear) with β-value of 350 using TOF and matrix size of 192 × 192.

4.3.3 Data Analysis

Data analysis was conducted within the QuantifyDCE software (Section 4.2.3) repeatably for all reconstructions, without altering the location of the input chamber and exchange cylinder spheres in any PET image, to minimize intra-observer errors.

Thereafter, the areas under the TACs (AUCs) were computed using Matlab (Mathworks Inc., version 2020b). In addition, the relative error of Qin and Qout values with respect to the reference flow value Qref were computed as follows

$$Flow\ value\ error = |(Flow\ value - Qref)/Qref * 100|. \quad (14)$$

4.4 Assessment of Various Injected Activities on MPI with a Flow Phantom (II)

This study included the D690 and DMI-20 systems as well as the flow phantom (details in Sections 4.1 and 4.2).

4.4.1 Data Acquisition

Data acquisition followed what has been explained in Section 4.3.1 with a difference that only one test was acquired on both systems and nine different activity levels were administered with both systems. The administered activities at the start of the scan are presented in Table 2.

Table 2. Administered activities measured at the scan start time (delay 50 seconds from injection). Modified from original publication I.

	Activity at Scan Start Time [MBq]	
Measurement	**DMI-20**	**D690**
1	325	359
2	488	400
3	546	532
4	621	607
5	655	729
6	691	833
7	906	995
8	1060	1130
9	1257	1230

4.4.2 Count-Rate Calculation

The number of scattered (S) events was calculated based on the parameter scatter fraction (SF) that corresponds the percentual relation between scattered events and the total number of events. SF is extracted from scatter correction for each time frame and saved in the DICOM header of the image. Therefore, the exact number of scattered events was calculated as follows

$$S = SF \cdot (P - R). \tag{15}$$

The estimated number of randoms (R) is extracted from each time frame in the DICOM header of the image. The estimated number of randoms is based on the

detected single events rate. *DTFs* was as well extracted individually from each time frame in the DICOM header of the image (Lewellen *et al.*, 1994).

4.4.3 Reconstruction

On DMI-20, OSEM-TOF-PSF with 3 iterations and 16 subsets with GFS of 5 mm and a FOV size of 35 cm was applied. The matrix size was 192 × 192.

On D690, OSEM-TOF-PSF with 2 iterations and 24 subsets with GFS of 5 mm and a FOV size of 35 cm was applied. The matrix size was 128 × 128.

All reconstructions included corrections for scatter, randoms, dead-time, attenuation, geometry, etc. The reconstructions follow the clinical protocol on both systems.

4.4.4 Data Analysis

Data analysis was conducted on both systems individually.

For each administered activity, at the time frame at peak *P*, peak *P*, *R*, *SF*, and *DTF* were extracted from the DICOM headers. The number of true and scatter events were thereafter calculated based on Equations (1) and (15). These parameters are called the peak count-rates.

TACs and flow values were extracted in repeatable manner with QuantifyDCE. A regression analysis was computed from modelled TACs with respect to tissue TACs. In addition, the relative errors of the flow values with respect to Qref were computed using Equation 14.

4.5 BSREM Evaluation in MPI (III)

This study included the DMI-20 system (details in Section 4.1).

4.5.1 Subject Population

This study used retrospective data from 179 patients who had undergone [^{15}O]H_2O MPI PET for suspected obstructive coronary artery disease (Table 3).

Table 3. Characteristics of 179 patients who had undergone [^{15}O]H_2O MPI PET for suspected obstructive coronary artery disease used in Study III. Modified from original publication III.

Descriptor	**Number**
Total Number of Subjects	179
Males	116
Females	63
Age (mean ± SD)	66 ± 10
Body-mass Index (kg/m^2) (mean ± SD)	30±6
Smokers (Current or previous)	75
Diabetics	35
Hypertension	98
Only Stress	162
Rest-Stress	17
Excluded	2

4.5.2 Data Acquisition

Data was acquired according to the clinical protocol (Maaniitty *et al.*, 2017). In stress PET acquisition, adenosine infusion (140 µg/kg/min) was started 2 minutes before PET acquisition, which was started 25 seconds after the target 500 MBq [^{15}O]H_2O bolus injection.

4.5.3 Reconstruction

Table 4. Reconstruction parameters used in Study III. Modified from original publication III.

Algorithm	**OSEM**	**BSREM**
TOF	TOF	TOF
PSF	PSF	PSF
Iterations	3	-
Subsets	16	-
Matrix Size	192 × 192	192 × 192
FOV	35 cm	35 cm
β-value	-	350

Patients' PET data was reconstructed using parameters in Table 4. Reconstructions included corrections for scatter, randoms, dead-time, attenuation,

geometry, etc. The reconstructions follow the clinical protocol on both systems. Reconstructions were conducted with the clinical PET/CT system workstation, using the software version pet_col_bb.31.

4.5.4 Data Analysis

Patients' PET data was analysed using Carimas 2.10 software (Turku PET Centre, Turku, Finland) by single observer. MBF values were quantitated based on the kinetic modelling for $[^{15}O]H_2O$. The basics of kinetic modelling are presented in Section 2.3 and are based on the studies by Iida *et al*. (Iida *et al.*, 1988, 1991, 1992). The initial guesses for the modelling parameters were: 0.5 ml/g/min for MBF, 0.5 for PTF, 0.5 for VL, 0.9464 for the partition coefficient, and 0.93 for the recovery coefficient. The myocardium was divided into 17 and three segments based on the standard by American Heart Association (Bom *et al.*, 2019). Three segments represent the standard myocardial territories for the coronary arteries: left anterior descending coronary artery (LAD), left circumflex coronary artery (LCX), and right coronary artery (RCA). Modelling parameters MBF (in units of ml/g/min), PTF (in units of ml/ml), and VL (in units of ml/ml) were extracted for each patient from each segment.

Patient was defined as ischemic if stress MBF < 2.3 ml/g/min occurred in at least two neighbouring segments (Danad *et al.*, 2014). Segments 2, 3, and 17 were left out from the analysis.

4.5.5 Statistical Analysis

Differences in MBF, PTF, and VL between the two reconstruction algorithms were analysed using two-tailed t-test, using $p < 0.05$ as the significance threshold.

4.6 Technical Factors Contributing the Reproducibility and Accuracy of Modelled Flow in MPI (IV)

This study included the DMI-20 and Vision-600 systems as well as the flow phantom (details in Sections 4.1 and 4.2).

4.6.1 Data Acquisition

The measurements included two sessions (test and retest) within two weeks on each system. Each measurement session applied 12 measurements, with three Qpump values and four constrictions for Qcyl for each Qpump. The peristaltic pump was

calibrated prior to each session. The data acquisition parameters for the measurements using the flow phantom are presented in Table 5. All PET acquisitions were started at the time of bolus injection.

Both DMI-20 and Vision-600 have their individual [^{15}O]H_2O bolus delivery systems (RadioWaterGenerator, RWG, Hidex Oy, Turku, Finland) installed beside the PET/CT gantry. The RWGs were calibrated using [^{15}O]H_2O prior each measurement session. The manufacturer guarantees 15% production accuracy to the requested dose. The requested activity was 500 MBq for all measurements. The administered activities for the first (test) and second (retest) measurement sessions were 488 ± 22 MBq and 472 ± 24 MBq for DMI-20 and 570 ± 22 MBq and 595 ± 16 MBq for Vision-600.

Table 5. Acquisition parameters of the flow phantom for all measurements in Study IV. Modified from original publication IV.

Measurement Qpump-Qcyl %		**Qcyl measured**				**Qtube measured**			
		DMI-20		Vision-600		DMI-20		Vision-600	
	Qpump	Test	Retest	Test	Retest	Test	Retest	Test	Retest
	[ml/min]	[ml/min]	[ml/min]	[ml/min]	[ml/min]	[ml/min]	[ml/min]	[ml/min]	[ml/min]
150-20%	150	31	30	32	30	124	127	125	111
150-40%	150	61	59	67	54	98	99	92	90
150-60%	150	91	94	93	79	63	61	62	60
150-80%	150	119	120	124	104	32	31	27	33
200-20%	200	41	43	40	41	171	168	168	154
200-40%	200	80	80	86	86	132	134	129	129
200-60%	200	126	131	115	114	83	80	82	83
200-80%	200	163	162	159	146	41	42	40	42
250-20%	250	49	47	55	52	200	203	205	194
250-40%	250	102	99	103	0	162	166	169	0
250-60%	250	153	160	159	133	103	100	108	101
250-80%	250	200	204	210	184	52	53	51	50

4.6.2 Reconstruction

All data was binned into 24 time frames 14 × 5 s, 3 × 10 s, 3 × 20 s and 4 × 30 s. All data corrections were applied.

Data reconstruction for DMI-20 was similar to Studies I, II, and III (OSEM-TOF-PSF) with FOV of 35 cm. On Vision-600 data was reconstructed using

Ordinary Poisson –OSEM (OP-OSEM) algorithm with TOF and PSF, 8 iterations, 5 subsets, matrix size of 220, 6 mm Gaussian post filter, and FOV of 35 cm.

4.6.3 Data Analysis

The sum of recorded Qcyl and Qtube were calculated and their relative differences to Qpump were computed. The administered bolus curves were extracted for all measurements and inspected visually. TACs and modelled flow values were extracted in repeatable manner using QuantifyDCE. The TACs were inspected visually. AUCs were computed from bolus curves and all TACs. In addition, the relative errors of the flow values with respect to Qref (Equation 14) as well as between test and retest measurements were computed.

5 Results

5.1 Effect of Reconstruction Parameters on MPI (I and III)

In Study I, the flow phantom OSEM-TOF-PSF reconstructions showed no visual differences in TACs when compared to BSREM (Q.Clear) reconstructions (Figure 3). Figure 3 highlights the differences in TACs measured from OSEM, OSEM-TOF, and OSEM-PSF reconstructions (Figure 3).

The errors of the flow phantom modelled flow values Qin and Qout with respect to Qref were smaller than 7% for all reconstructions (Figure 4). Qin errors were larger compared to Qout errors for all reconstructions. OSEM and OSEM-PSF reconstructions resulted in the smallest Qout erros.

In Study III, the patient studies, the BSREM reconstruction resulted in similar ($p > .05$) kinetically modelled clinical parameters MBF, PTF, and VL when compared to OSEM-TOF-PSF reconstruction. The relative differences between BSREM and OSEM-TOF-PSF were smaller than 4%, 2%, and 6% for stress studies and 7%, 4%, and 6% for rest studies, for MBF, PTF, and VL, respectively. In addition, the regression analysis showed strong correlation between BSREM and OSEM-TOF-PSF with R^2 values being 0.97, 0.97, and 0.98 for the 17-segment polar maps and 0.98, 0.93 and 1.0 for three-segment polar maps, respectively for ischemic, non-ischemic, and rest subjects.

However, the classification of myocardial ischemia resulted in different number of ischemic subjects on the BSREM reconstruction compared to OSEM-TOF-PSF reconstruction. BSREM classification resulted in 113 (out of 117) ischemic subjects and in 115 ischemic subjects on OSEM-TOF-PSF, based on the 17-segment polar maps. Therefore, 99% of subjects were classified similarly, with two outliers. However, the three-segment polar map classification resulted in the same number of ischemic and non-ischemic subjects between BSREM and OSEM-TOF-PSF.

In the first subject with discrepant classification, BSREM classified one segment ischemic, compared to OSEM-TOF-PSF classifying four segments ischemic. The polar maps from the first subject are presented in Figure 5. For the second subject, BSREM classified two segments ischemic, and OSEM-TOF-PSF five. Visually, the polar maps appear similar between BSREM and OSEM-TOF-PSF (Figure 5).

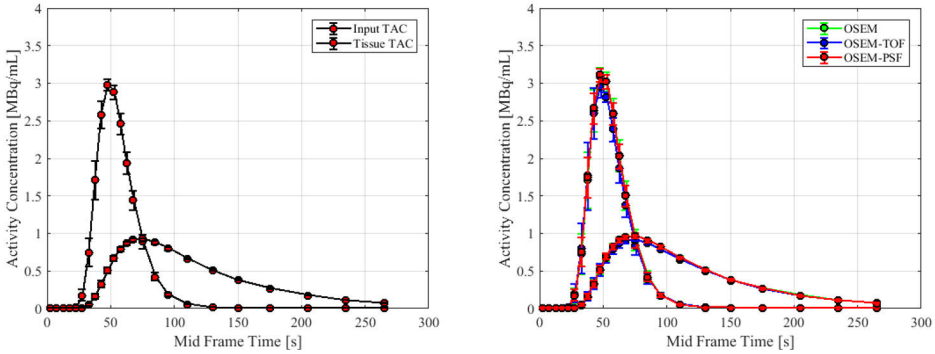

Figure 3. Input and tissue time-activity curves (TAC) presented for the BSREM (Q.Clear) (left) and OSEM, OSEM-TOF, and OSEM-PSF reconstructions (right). In left the TACs are similar to OSEM-TOF-PSF reconstructions with different matrix sizes and GFS values and thus, are not shown separately. From original publication I.

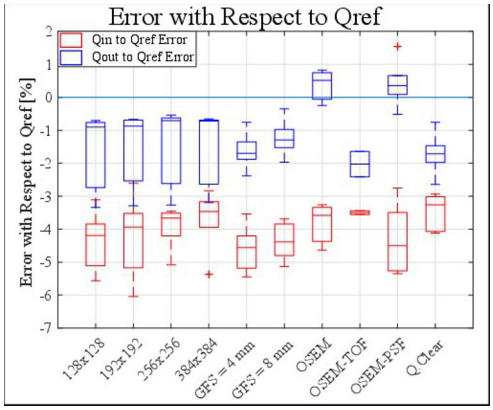

Figure 4. Relative error values of the flow values with respect to Qref. From original publication I.

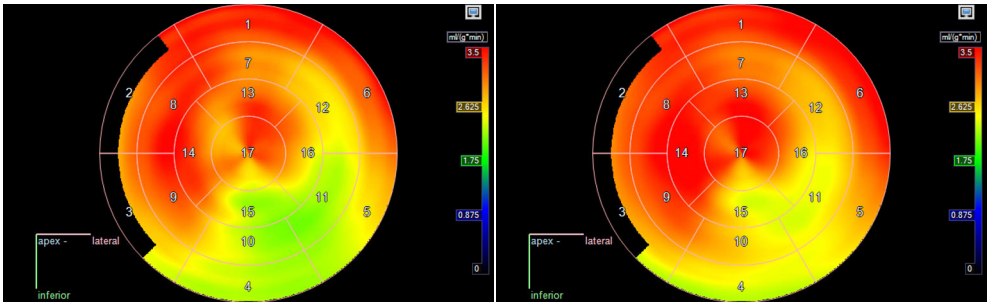

Figure 5. OSEM-TOF-PSF (left) and BSREM (right) polar maps presented for the first subject with discrepant classification of ischemia. OSEM-TOF-PSF classified the subject ischemic, BSREM as non-ischemic. From original publication III.

5.2 Assessment of Various Injected Activities on MPI with a Flow Phantom (II)

In Study II, the various injected activities resulted in higher count-rates on the digital system (DMI-20) compared to the analog system (D690). The highest peak prompts were measured at 12.8 Mcps with the activity at scan start time of 1257 MBq on the digital system (DMI-20). The corresponding numbers for the analog system (D690) were 6.85 Mcps at 1230 MBq (Figure 6). With the highest injected activity on DMI-20, the scattered and true counts decreased compared to other measurements (Figure 6b). Similar behaviour was not seen on D690 on which all count-rates increased linearly.

*DTF*s increased linearly with respect to injected activities (Figure 7a). *DTF*s corresponding the highest injected activities were 2.06 and 1.57 on DMI-20 and D690, respectively.

*SF*s increased linearly on D690 up to all injected activities (Figure 7b). On DMI-20, *SF*s also increased linearly but stabilized up to the three highest injected activities and were nearly similar for them.

TACs were similar between DMI-20 and D690 for all injected activities and showed no visual distortions (Figure 8). Two-compartmental model fitting produced R^2 values 0.998 and 0.999 on DMI-20 and D690 for all measurements.

The errors of Qin with respect to Qref were of similar magnitude for all injected activities on both systems (Figure 9). However, Qout error values increased when the injected activity increased on both systems. On the highest injected activity, Qout error value was higher for DMI-20 compared to D690, with values of -12.4% and -7.12%, respectively.

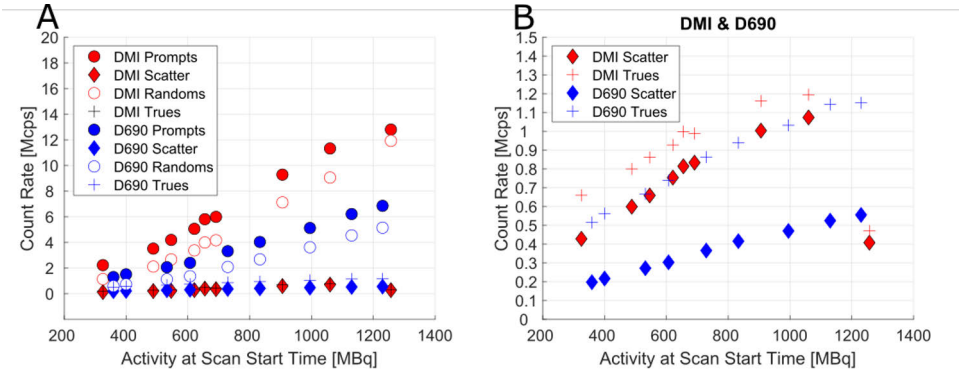

Figure 6. **A)** Peak count-rates measured across various injected activities for DMI-20 and D690. **B)** Zoomed-plot for the peak scattered and true counts as a function of activity at scan start time. From original publication II.

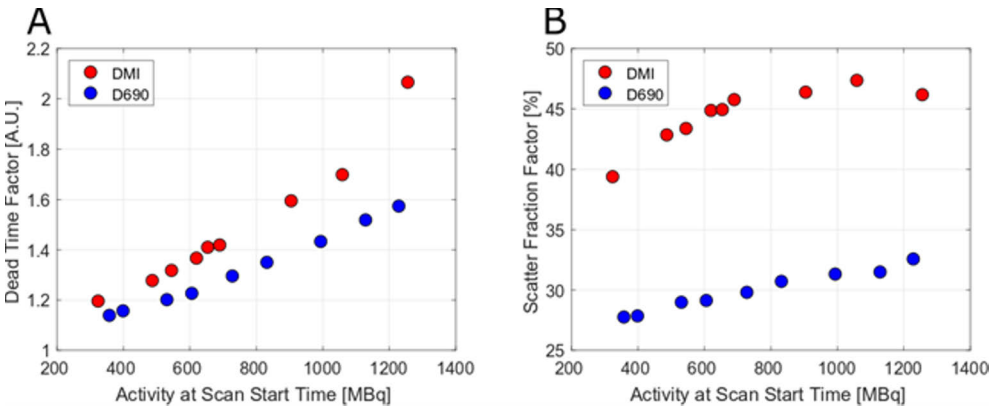

Figure 7. **A)** Dead-time correction factors (*DTF*s) and **B)** scatter fraction factors (*SF*s) at peak prompts as a function of activity at scan start time for DMI-20 and D690 flow phantom measurements. From original publication II.

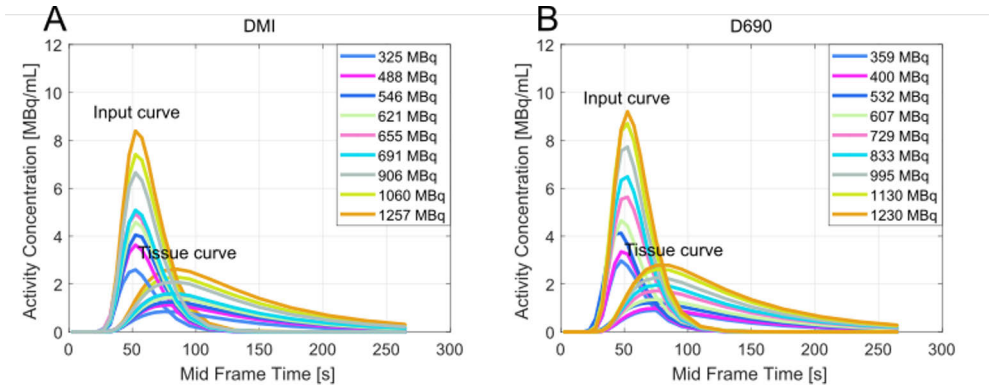

Figure 8. Input and tissue TACs measured across various injected activities for **A)** DMI-20 and **B)** D690. From original publication II.

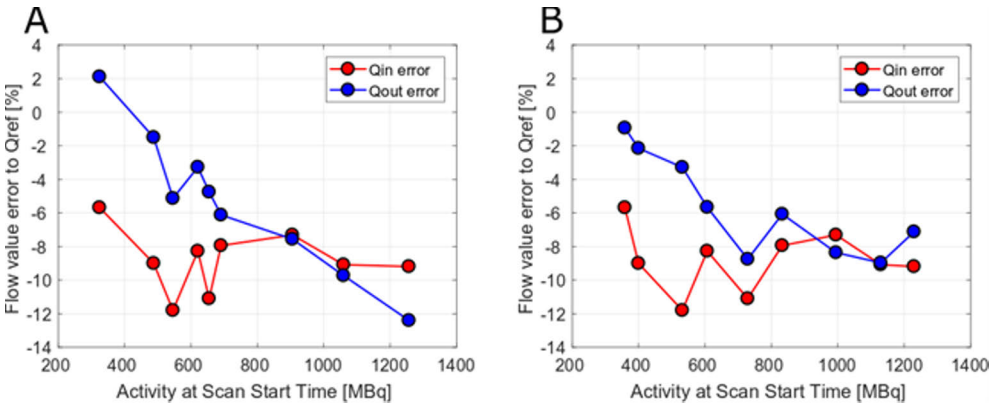

Figure 9. Qin and Qout relative error values for **A)** DMI-20 and **B)** D690 as a function of activity at scan start time. From original publication II.

5.3 Technical Factors Contributing the Reproducibility and Accuracy of Modelled Flow in MPI (IV)

In Study IV, the technical factors evaluated were the effect of the flow meter recordings during the flow phantom studies and the contribution from the RWGs to the modelled flow values Qin and Qout.

The sum of flow meter recording differences (Qtube+Qcyl difference with respect to Qpump) resulted into smaller than 10% differences for all measurements on both DMI-20 and Vision-600 (Figure 10). In addition, the injected bolus curves extracted from RWGs were similar between test and retest measurements on both systems (Figure 11). Measurements on Vision-600 however produced higher bolus peaks compared to measurements on DMI-20. That resulted into higher bolus AUCs (not shown here), input TAC peaks as well as input AUCs (not shown here).

Despite of higher input TAC peaks on Vision-600, all TACs were otherwise visually similar between test and retest measurements as well as systems on most measurements (Figures 12 and 13). One measurement on DMI-20 showed visually different tissue and modelled TACs (250-80%), and three measurements showed visual differences on Vision-600 (150-20%, 150-80%, and 200-80%) between test and retest measurements.

When comparing the repeatability of the measurements, the test-retest Qin and Qout relative errors on the measurements on DMI-20 were smaller than 15% on all measurements whereas on Vision-600 the errors exceeded 15% on half the measurements due to bolus injections (Figure 14). When comparing the reproducibility and accuracy of the measurements between the systems, the Qin and Qout relative errors with respect to Qref were smaller on the measurements on DMI-20 compared to the measurements on Vision-600 (Table 6). In particular, the measurements on Vision-600 produced higher Qin errors compared to DMI-20, several being larger than 10%. This follows from the higher bolus and input TAC peaks, which affect more to the modelled value Qin.

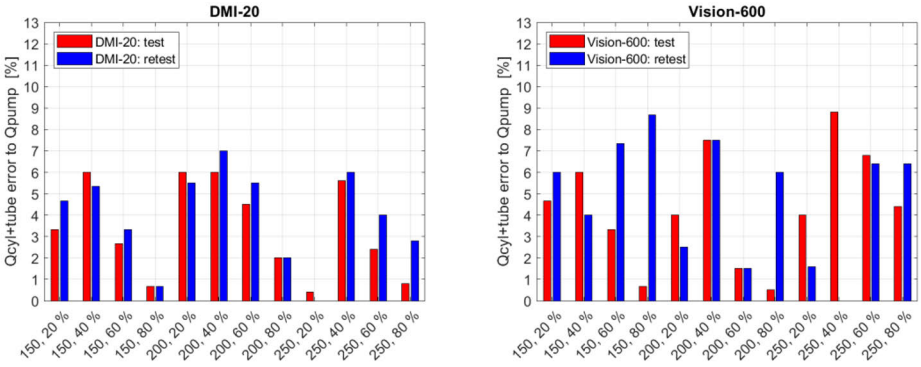

Figure 10. Qcyl+Qtube relative errors with respect to Qpump presented for all measurements on DMI-20 (left) and Vision-600 (right). From original publication IV.

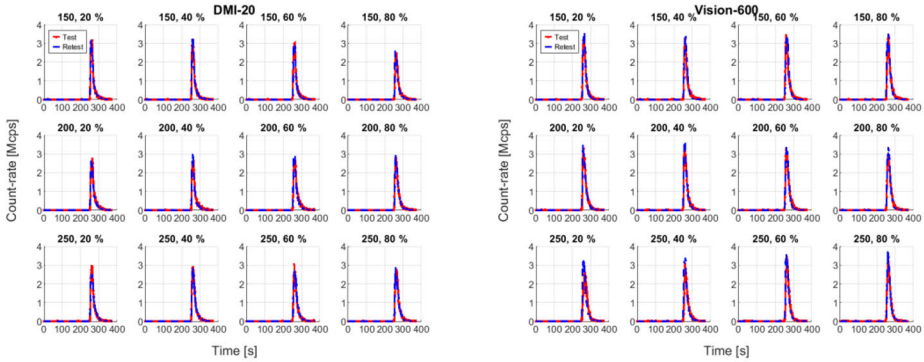

Figure 11. [^{15}O]H_2O bolus curves extracted for each measurement on the RWG system installed on DMI-20 (left) and Vision-600 (right). From original publication IV.

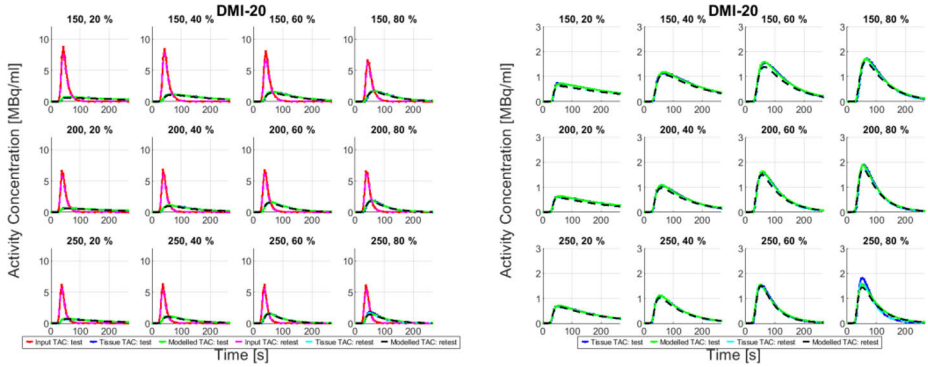

Figure 12. Input, tissue, and modelled time-activity curves (left), and zoomed tissue and modelled TACs (right) recorded on DMI-20 from all measurements. From original publication IV.

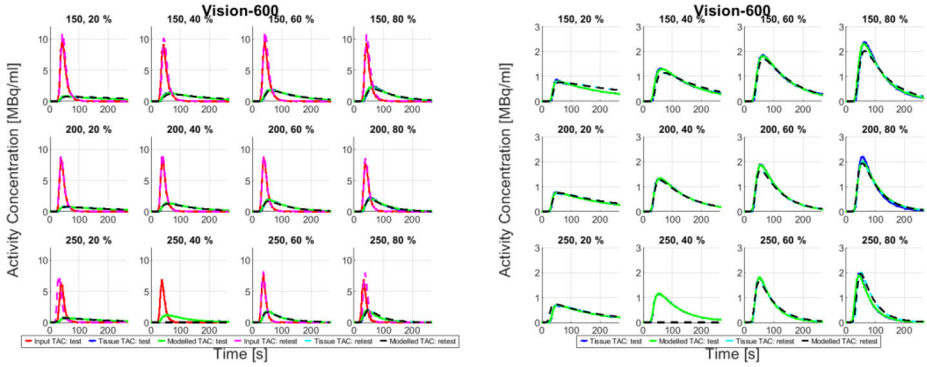

Figure 13. Input, tissue, and modelled time-activity curves (left), and zoomed tissue and modelled TACs (right) recorded on Vision-600 from all measurements. From original publication IV.

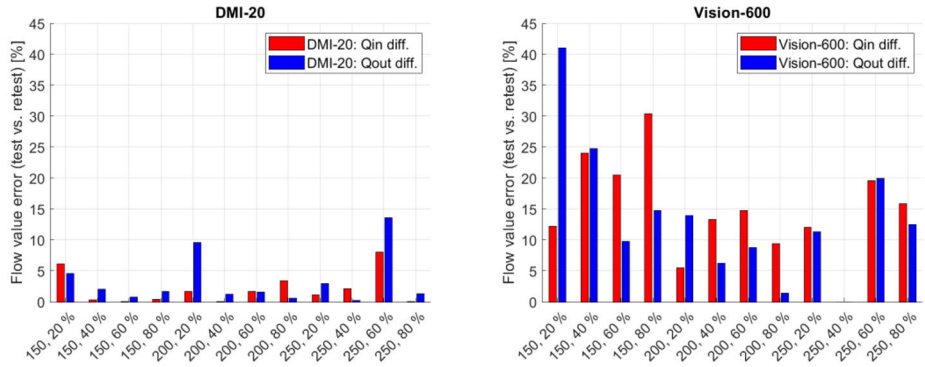

Figure 14. Qin and Qout differences between test and retest measurements on DMI-20 (left) and Vision-600 (right). From original publication IV.

Table 6. Absolute relative errors of modelled Qin and Qout with respect to Qref from all measurements on both DMI-20 and Vision-600. Modified from original publication IV.

Measurement	DMI-20		Vision-600		DMI-20		Vision-600	
	Qin error		Qin error		Qout error		Qout error	
	Test	Retest	Test	Retest	Test	Retest	Test	Retest
	%	%	%	%	%	%	%	%
150-20%	19	23	25	31	22	24	3	40
150-40%	8	6	9	19	19	15	7	18
150-60%	2	1	4	12	2	4	6	2
150-80%	6	5	9	10	0	1	2	1
200-20%	15	17	18	24	27	22	15	28
200-40%	2	2	8	12	3	4	5	1
200-60%	9	3	4	11	7	2	9	0
200-80%	2	5	11	12	3	3	9	1
250-20%	4	6	12	19	3	3	13	20
250-40%	1	-	4	-	1	-	3	-
250-60%	2	5	1	4	1	9	11	8
250-80%	22	23	7	13	23	26	1	1

6 Discussion

6.1 Effect of Reconstruction Parameters on MPI (I and III)

Studies I and III evaluated the effect of reconstructions on the quantitative accuracy of modelled parameters derived both from flow phantom as well as patient PET images. In flow phantom studies, the effect was studied in terms of TACs and the modelled flow values, Qin and Qout. In patient studies, the effect was studied in terms of the clinical modelled parameters, MBF, PTF, and VL, as well as the myocardial ischemia classification concordance between reconstructions.

In general, both flow phantom and patient studies resulted in similar findings. The OSEM-TOF-PSF reconstruction was in concordance with the BSREM (Q.Clear) reconstruction in terms of flow phantom derived TACs as well as modelled parameters Qin and Qout. Similarly, high agreement was measured for non-ischemic, ischemic, and rest subjects between the reconstructions. Also, the classification was similar in 99% of the patients between the reconstructions. Therefore, these findings complement each other, and indicate that BSREM (with β=350) can be reliably applied in patient MPI for myocardial ischemia classification with [^{15}O]H_2O.

Study III also indicates that either BSREM or OSEM-TOF-PSF reconstruction can be reliably used for diagnosing the myocardial viability, as PTF plays a role in differentiation of viable myocardium for infarct scar (Grönman *et al.*, 2021). However, for PTF, larger effects might be observed across different reconstructions, as the tissue fraction might vary within the constant delineated VOI when PVE alters. However, Nordström *et al*. showed that the effect on PTF could be minimal across different reconstructions (Nordström *et al.*, 2022). This effect should still be confirmed with further investigations.

When it comes to ischemia classification, BSREM and OSEM-TOF-PSF resulted in different classification on two subjects based on the threshold of ischemia that has been previously defined by Danad *et al*. (Danad *et al.*, 2014). BSREM classified the subjects non-ischemic and OSEM-TOF-PSF ischemic. However, the visual interpretation from the BSREM polar maps indicated only very small

differences to OSEM-TOF-PSF for these subjects (Figure 5) caused by random noise and MBF variability close to the threshold of ischemia.

In general, the consistency between BSREM and OSEM-TOF-PSF is probably due to the fact that the kinetic model of [^{15}O]H_2O relies on the k2 estimate and therefore results in stable MBF quantification across various image noise levels, as Nordström et al. recently discussed (Nordström *et al.*, 2022). When compared to other perfusion tracers, such as [^{82}Rb] and [^{13}N]NH_3, their kinetic models rely on K1 estimate (Muzik *et al.*, 1993; Prior *et al.*, 2012). Christensen et al. however indicated that BSREM can be used for [^{82}Rb] (Christensen and Tolbod, 2017) and O'Doherty et al. showed that [^{13}N]NH_3 MBF quantification is minimally affected when using BSREM (O'Doherty *et al.*, 2017). Therefore, these are in line with our findings.

In flow phantom studies, the non-TOF-PSF reconstructions resulted in different TACs (Figure 3) and flow value errors (Figure 4) compared to TOF-PSF-reconstructions, following the results from previous studies (Presotto *et al.*, 2015; Matheoud *et al.*, 2017). TOF reconstruction results in faster convergence rate in most objects compared to non-TOF reconstruction (Surti *et al.*, 2006; Karp *et al.*, 2008; Surti, 2015; Vandenberghe *et al.*, 2016). Therefore, TOF reconstructions have overall better noise handling properties compared to non-TOF reconstructions. Iida et al. (Iida et al., 1992) have shown that added noise in input function results into bias and variance in the modelled flow values. In addition, Kero et al. showed that non-TOF reconstruction produces higher MBF values compared to TOF reconstruction (Kero et al., 2017). Therefore, in clinical MPI, TOF-reconstructions are beneficial as they have better noise-handling properties.

The results of these studies are in line with several previous studies. Kero *et al*. showed minor dependence of the selection of reconstruction parameters on MBF quantification (Kero *et al.*, 2017). The largest variations measured in Study I and III were smaller than 7% for any parameter between reconstructions in flow phantom and patient studies. This is also in line with the studies from El Fakhri et al. and Johansson et al. that measured 16% and 15% reproducibility in MPI (Johansson *et al.*, 2004; El Fakhri *et al.*, 2009). What is more, O'Doherty *et al*. indicated that OSEM-TOF-PSF noise level is similar to BSREM ($\beta = 300$) noise level and that BSREM is highly correlated ($p > .95$) across other reconstructions (O'Doherty *et al.*, 2017). We showed similar findings both in flow phantom and patients studies for OSEM-TOF-PSF and BSREM ($\beta = 350$). Similarly, Nordström *et al*. also indicated that only minor effects appear in MBF quantification if BSREM uses any β-value within the range 100–1000 (Nordström *et al.*, 2022). We applied only one β-value (350) due to the retrospective nature of our study. The β-value used in this study is routinely applied in MPI studies at our institute and is the default value set in the Discovery MI 20 4-ring system. These findings are however supported by the results from the studies by Armstrong *et al*. and Germino *et* al. that showed positive effect

on MBF quantification when including TOF and PSF (Armstrong, Tonge and Arumugam, 2014; Germino *et al.*, 2016). Therefore, the findings from Study I and III indicate that [^{15}O]H_2O MPI is quantitatively accurate and reproducible when using BSREM.

6.2 Assessment of Various Injected Activities on MPI with a Flow Phantom (II)

Study II assessed the quantification accuracy of the digital (DMI-20) and analog (D690) PET/CT system for [^{15}O]H_2O myocardial perfusion imaging across various injected activities using a flow phantom.

As expected, overall the count-rates were higher with the digital DMI-20 system, compared to the analog D690 system. The maximum count rate was 12.8 Mcps with DMI-20, the corresponding number being 6.85 Mcps for D690, with similar injected activity. However, on DMI-20 there was a sudden notch in scatter and trues rates with the highest injected activity. This is due to the fact that DMI-20 limits the amount of data transmitted for histogramming above a system-specific throttle limit. The limit for DMI-20 is 12.8 Mcps, which was reached during the acquisition with the highest injected activity. However, this throttle limit is taken into account in the reconstruction process, as the number of prompts limited by the throttle are eventually scaled up. In clinical practice this means that MPI quantitative accuracy remains reliable up to the counting levels investigated in Study II. What must be noted is that this study did not include the calculation of NECR curves. This is because the NECR curves would have given misleading information as they would not have been comparable to NECR curves measured in NEMA tests.

*DTF*s and *SF*s were higher for DMI-20 compared to D690. *DTF*s increased linearly over all injected activities for both systems but *SF*s stabilized within the three highest injected activities on DMI-20. The SF behaviour is likely caused by biased scatter scaling at high activities by counts outside the body contour or by increased detector scatter, which is usually seen in NEMA testing (Hsu *et al.*, 2017). However, scatter overcorrection should not be possible in this study, as there was no CTAC-PET misalignment. In patient studies, misalignment may however occur and therefore *SF*s at very high count-rates should be further studied in clinical MPI.

When it comes to flow quantification accuracy, overall the Qin and Qout errors to Qref were similar between DMI-20 and D690. With the highest injected activity, Qout error was -12% on DMI-20 and -7% on D690. This might be due to the very high activity present in the system within the first time frames on DMI-20, affecting the Qout quantification. The cause for this effect should however be confirmed with even higher injected activities. Therefore, this caused a limitation to this work, as no higher than 1257 MBq activity at scan start time was possible to produce with the

[^{15}O]H_2O bolus delivery system. This fact should be taken into account especially if applying [^{82}Rb] as a tracer, as its injected activity may exceed 1200 MBq (Hesse *et al.*, 2008; Dilsizian *et al.*, 2016; Murthy *et al.*, 2018). In addition, if applying other DMI systems in MPI, such as DMI-25, which has even higher sensitivity than DMI-20, the flow quantification accuracy should be confirmed on those systems as well. This also applies on any other PET system.

When comparing the results of this study to other studies, some differences appear. For example, O'Doherty *et al*. and Lassen *et al*. showed distortions in TACs with [^{18}F]F^- and [^{82}Rb] above 594 MBq and 1006 MBq, respectively (O' Doherty *et al.*, 2017; Lassen *et al.*, 2020). In our study, TACs showed no distortions even with the highest injected activities. In addition, the largest error measured in this study (-12%) was not as high as measured by Lassen *et al*. (22%) (Lassen *et al.*, 2020). However, the count-rate performance results in this study are in line to what has been reported previously (deKemp *et al.*, 2008; O' Doherty *et al.*, 2017; Renaud *et al.*, 2017; van Dijk *et al.*, 2019). Those studies showed higher count-rates and *DTF*s with systems with higher sensitivities, similarly as the digital DMI-20 system compared to the analog D690 system in this study. Nevertheless, these flow phantom studies should be conducted on other perfusion tracers such as [^{82}Rb] and [^{13}N]NH_3 as well, in order to confirm the applicability of these results for other perfusion tracers.

6.3 Technical Factors Contributing the Reproducibility and Accuracy of Modelled Flow in MPI (IV)

Study IV assessed the contribution of technical factors to the reproducibility and accuracy of modelled flow values using the flow phantom. This study has an intent to be used for harmonization measures in the future using this preliminary protocol as basis. The evaluation included two digital PET/CT systems but analog systems could also be added in the evaluation. Overall, the measurements were highly repeatable as the repeatability errors of Qin and Qout were smaller than 15% on all measurements on DMI-20 and on half measurements on Vision-600 (Figure 14).

The first technical factor analyzed was the sum of recorded flow values (Qcyl+Qtube) during the flow phantom studies. Ideally the recorded Qtube+Qcyl shoud be equal to Qpump. Even though there were differences in most measurements on both systems, the overall differences were smaller than 10% (Figure 10). Therefore, the flow phantom itself presumably has minor direct effect on the modelled flow values.

The second technical factor analyzed was the contribution from RWGs. This analyzation confirmed whether the bolus administration has direct effect on the modelled flow values. Overall, bolus administrations were repeatable between test

and retest measurements on both systems (Figure 11). When comparing the systems, the RWG of Vision-600 produced higher bolus peaks and therefore affected increasingly on the bolus AUCs, input TAC peaks (Figure 13), and input AUCs when compared to the RWG of DMI-20 (Figure 12). Therefore, this finding showed that the RWG bolus administration has direct impact on the input TAC. This finding is explained by the fact that the administered bolus travels directly from the flow phantom injection port to the flow phantom input chamber without mixing or dispersion on the way, with relatively short distance and time. Therefore, the contribution from the RWG bolus administration contributes to input TAC and finally the accuracy of modelled flow values. This is seen as Qin and Qout error differences between the systems (Table 6). Iida *et al*. have also reported that noise in input function may cause bias in the calculated parameters (Iida *et al.*, 1992).Therefore, our results are in line with the study by Iida *et al*. (Iida *et al.*, 1992).

Eventually, the RWG bolus administration affects more Qin compared to Qout (Table 6), as Qin relies on the K1 modelling parameter and is therefore more sensitive for variations in TACs, as discussed by Kero et al. (Kero *et al.*, 2017). In clinical practice this means that MBF quantification reproducibility and accuracy between systems may be limited by the repeatability of bolus injections, among other factors. This study highlights the importance for harmonized bolus administrations and conducting reproducibility and accuracy investigations for multi-centre MPI. Based on the findings, it is also recommended that patient MPI should be conducted on single system as long as there is no MPI harmonization protocol available.

This study was limited by the reconstructions between the Vision-600 and DMI-20 systems. However, the reconstructed voxel sizes were similar between the systems (DMI-20: (x, y, and z) 1.82 mm, 1.82 mm, and 2.79 mm, Vision-600: 1.65 mm, 1.65 mm, and 3 mm). Harmonizing the reconstruction parameters should also be studied in the future.

When comparing the results of this study to previous investigations, the repeatability of modelled flow values on single system (less than 15% difference in most measurements) are within similar range to what has been clinically reported for [^{15}O]H_2O. For example the table in Klein et al. (Klein *et al.*, 2018) describes that overall the stress MBF values have repeatability accuracy from 11% to 34%, and for [^{15}O]H_2O the reported values are 27% (Wyss *et al.*, 2003) and 25% (Kaufmann *et al.*, 1999). These findings also follow what has been reported for SUV repeatability. There is 10% coefficient of variation for SUV (SUVmean, SUVpeak, SUVmax) (Lodge, 2017) with reproducibility rates of 27% for SUVmean and SUVpeak and 33% for SUVmax (Koopman *et al.*, 2019) with [^{18}F]FDG. Several studies have also evaluated the repeatability of myocardial perfusion studies for [^{13}N]NH_3 and [^{82}Rb] that resulted into similar rates as for [^{15}O]H_2O and the measurements presented in this study (Suda *et al.*, 2016; Monroy-Gonzalez *et al.*, 2020; Byrne *et al.*, 2021).

Direct comparison to [^{13}N]NH_3 and [^{82}Rb] was however was not possible in this study as such tracers are not available at our institute. In conclusion, the flow phantom repeatability results in this study agree well with the results gained from previous clinical studies. However, this study showed limitations between systems in terms of reproducibility and accuracy due to bolus administrations. Therefore, it is important to ensure systematic bolus administrations between systems.

6.4 Summary of the Findings

In this thesis, several investigations evaluated the digital PET system capabilities in [^{15}O]H_2O myocardial perfusion imaging. Reconstruction techniques were evaluated both in phantom studies and retrospectively with MPI patients. The novel reconstruction technique, BSREM, was shown to be highly concordant with other reconstruction techniques that have been routinely used in MPI. Therefore, it can be reliably used in clinical studies. In addition, system performance was assessed with the digital and analog PET systems across various injected activities and showed that clinical MPI can be conducted reliably when injected dose is smaller than 1200 MBq on either digital or analog PET system. Therefore, the current injections with 500 MBq of [^{15}O]H_2O in Turku PET Centre create acceptable count-rate levels on the digital DMI-20 system. And finally, the technical factors contributing to the modelled flow values were evaluated showing the most significant factor being the [^{15}O]H_2O bolus injector system. In general, these findings indicate that, clinical MPI PET benefits on incorporating digital PET systems and BSREM reconstructions but needs a standard tracer injector protocol as well as future assessments of harmonized clinical protocols across PET systems and centers.

6.5 Limitations

There are several limitations in these studies. First, these studies were mainly conducted using two software, the one being QuantifyDCE specifically designed for the flow phantom quantitative analysis, and the other being Carimas 2.10, available for clinical MPI analysis. These studies could have benefit from using other commercial software available for clinical use, also. However, previous study has shown that Carimas is repeatable and agrees well with other software tools (Harms *et al.*, 2014). In addition, our studies complement for example the study by Nordström *et al.*, who recommended repeating the reconstruction analysis with different software tools in order to confirm their investigations (Nordström *et al.*, 2022).

Second, these studies did not include inter- or intra-observer repeatability analyses either in flow phantom or clinical studies. However, we have previously

studied intra-observer repeatability with the flow phantom and showed no clear repeatability differences (Siekkinen *et al.*, 2019). Futhermore, the flow phantom quantitative analysis is built highly repeatable in the QuantifyDCE software as the software automatically defines the VOI size and location. Therefore, the user only must choose the starting point for the VOI search. Although, as this selection obviously depends on the user it might influence the final analysis. This could be studied more efficiently in the future. When it comes to the clinical MPI, Nesterov *et al*. have already showed MPI analyses to vary 9% and 10% within intra- and inter-observers with Carimas, respectively (Nesterov *et al.*, 2009). Therefore, the clinical intra- and inter-observer variability in our studies rely on those measurements.

6.5.1 Flow Phantom

The most extensive limitations of these studies appear within the flow phantom. In general, the flow phantom has been designed as a methodological reference standard. Therefore, it does not fully mimic the myocardial tissue, or the body background attenuation. What is more, the kinetic modelling of the flow phantom is not fully comparable to its clinical counterpart developed by Iida *et al* (Iida *et al.*, 1988, 1991, 1992). In addition, the flow phantom simplifies the physiological blood perfusion and tracer circulation in heart. However, Gabrani-Juma *et al*. have validated this flow phantom for MPI reference purposes, and the Qin and Qout parameters offer feasible reference values, a.k.a. the ground truth solutions for K1 and k2 parameters (Gabrani-Juma *et al.*, 2017). Therefore, the flow phantom offers a reliable standard for reproducible methodological MPI PET investigations, as these studies have shown.

What is more, ideally, the flow phantom should fulfill Equation 7, which determines that the flow defined by peristaltic pump should equal to Qtube and Qcyl measured at the flow meters, together. However, for example in Study I, Qtube and Qcyl result in 219 ml/min together on average, that is not equal to 200 ml/min, defined at the peristaltic pump. This effect might be due to several issues: there might have been a large air bubble within the system that blocked a hose and therefore lifted up the pressure in another hose and thereafter raised the water flow, or the hoses could have been at different levels that may have raised pressure in another hose and thereafter raised the water flow, or the pump might have been inaccurately calibrated, or the calibration factor might have not been longer valid whenever the flow meter values were recorded. Nevertheless, this effect is taken into account during the quantitative analysis in the QuantifyDCE software, which requires inserting the flow meter calibration curve prior to image analysis. Therefore, we consider this effect is negligible, as also explained for Study IV.

When it comes to modelled flow values, all the studies showed that in general the errors of the Qin parameter with respect to Qref were larger compared to the errors of the Qout parameter. Their difference to Qref was 9 ml/min, on average. Qin and Qout are modelled from the wash-in (K1) and wash-out (k2) clearance rates of the tracer, respectively. Qout is determined from the exponential term (k2), making it less susceptible for variations in activity, as explained in the study of Kero *et al*. (Kero *et al.*, 2017). Therefore, image noise levels and thereafter for example the selection of reconstruction parameters have clearer impact on Qin compared to Qout.

In the future, these limitations could be minimized by developing the flow phantom physiological simulation. For example, by improving the exchange cylinder to have more homogeneous tracer perfusion and distribution. Thereafter, the kinetic modelling approximation would be closer the clinical counterpart and tracer dispersion and mixing would mimic blood perfusion more reliably.

6.6 Future Prospects

These studies offer primary understanding of the technical factors affecting MPI PET as well as an highlight the important basis for assessing standardization procedures in [^{15}O]H_2O MPI PET, especially in multi-center studies.

To start with, the flow phantom studies should be continued in order to provide a simple daily quality control protocol that could be easily applied in MPI PET in a similar fashion what is currently routinely performed for [^{18}F]FDG oncology imaging with static phantoms. These investigations could be started by designing a standard and systematic protocol for bolus administrations across different delivery systems, using the findings from Study IV as basis. Thereafter the investigations could aim at fundamental and extensive uncertainty investigations of other factors affecting MBF quantification reproducibility and accuracy across centres. The factors investigated would include the various analysis software, acquisition protocols, and PET systems. Finally, the results from the uncertainty analysis would allow proposing acceptable limits of variation for the modelling parameters, such as for the Qin and Qout parameters, for daily quality control of MPI quantification accuracy. This is however not straightforward as the PET system performance varies across different systems. Therefore, the quality control protocol should contain limits for different generation systems with similar detector techniques. The multi-center studies could aid establishing these kinds of system-specific limits.

More extensively speaking, total-body PET is the contemporary application for PET, and will probably replace the common whole body PET systems in the future (Nadig *et al.*, 2022). Therefore, studies, similar as performed in this thesis, should be conducted for those systems as well, in order to ensure the accuracy of MPI studies. This suggestion applies also for other longer axial FOV PET systems with

high sensitivity. This is important especially when using perfusion tracers with short half-life and high initial injected activity, such as [^{82}Rb] that applies over 1100 MBq in MPI PET (Dilsizian *et al.*, 2016).

Not only total-body PET but kinetic modelling in general will be more extensively used in the future. For example, brain perfusion studies using [^{15}O] as the tracer isotope would benefit from evaluating the digital PET system performance and quantitative accuracy in a reproducible manner, using a test object capable of simulating brain perfusion in dynamic manner.

7 Conclusions

1. The effect of matrix sizes, Gaussian filter sizes, TOF and/or PSF as well as BSREM (Q.Clear) reconstruction to image-derived flow values causes smaller than 7% error to the reference flow with DMI-20 using $[^{15}O]H_2O$.

2. DMI-20 and D690 preserved accurate flow quantification over all injected activities, with maximum error of 12%.

3. OSEM-TOF-PSF and BSREM image reconstructions produce similar MBF values and diagnosis of myocardial ischemia in patients undergoing $[^{15}O]H_2O$ PET due to suspected obstructive coronary artery disease.

4. A preliminary protocol for measuring the accuracy and reproducibility of flow values in $[^{15}O]H_2O$ MPI with two individual injector systems on the flow phantom measurements conducted with the DMI-20 and Vision-600 systems creates test-retest reproducibility below 15% on all measurements on DMI-20 and on half of the measurements on Vision-600. This study highlights the importance of implementing a standardized bolus injection and delivery protocol, which should be carefully investigated in a multi-centre setting.

Acknowledgements

This study was carried out within the Finnish Center of Excellence in Molecular Imaging in Cardiovascular and Metabolic Research at the Turku PET Centre, Department of Clinical Physiology and Nuclear Medicine (KLIP) in Turku University Hospital and University of Turku, Turku, Finland during the years 2019-2023. I want to thank Urho Känkänen Foundation (Urho Känkäsen säätiö), Paavo Nurmi Foundation (Paavo Nurmen Säätiö), Turku University Foundation (Turun Yliopistosäätiö), Hospital District of Southwest Finland (EVO funding, project numbers 11209 and 13236), University of Turku Graduate School (UTUGS) the Doctoral Programme in Clinical Research, EMPIR programme and the European Union's Horizon 2020 research and innovation programme (15HLT05 PerfusImaging, 19SIP04 Trac-PETperf), Academy of Finland (Grant No. 314483, Project MINMOTION), KLIP, Sairaalafyysikot ry, Turku University Foundation, and CompLifeSci Research Program for financially supporting this study.

I express my deepest gratitude to my primary supervisor, Jarmo Teuho. Thank you for always trusting in me, for giving me the opportunities and for helping me whenever I needed help. You have a great soul. Second, I want to thank my other supervisor, Mika Teräs. Thank you for always supporting me, and thank you for giving me the most valuable gift of all, the opportunity to become medical physicist. I also want to acknowledge my third supervisor Antti Saraste. Thank you for always being open for questions and giving my research the valuable clinical perspective.

Thereafter, I thank my co-authors; Tuula, Virva, Hidehiro, Kalle, Juhani, Chunlei, Teemu, Anna, Linda, Heidi, Nadia, and Andy. The value of your help is unmeasurable. Also is unmeasurable the kindness and support I have always received in Turku PET Centre, which I'm proud to call my research home. I thank you all. In addition, I thank my fellow physicists in Tyks, it is a privilege to be able to call you colleagues. I also express my gratitude to our beloved MINMOTION group. Thank you, Mojtaba, Juho, Riku.

And thank you Pirkko and Jouko, you have given me a great example how to live life. And of course, thank you Mervi and Jari, your support in my life is the greatest of all.

And thank you for everything, Eero.

Turku, 07.08.2023
Reetta Siekkinen

References

Aide, N. *et al.* (2017) 'EANM/EARL harmonization strategies in PET quantification: from daily practice to multicentre oncological studies', *European Journal of Nuclear Medicine and Molecular Imaging*, 44, pp. 17–31. doi: 10.1007/s00259-017-3740-2.

Antonini, A. (2010) 'SPECT Imaging in Movement Disorders', *Encyclopedia of Movement Disorders*, pp. 140–147. doi: 10.1016/B978-0-12-374105-9.00074-5.

Armstrong, I. S., Tonge, C. M. and Arumugam, P. (2014) 'Impact of point spread function modeling and time-of-flight on myocardial blood flow and myocardial flow reserve measurements for rubidium-82 cardiac PET', *Journal of Nuclear Cardiology*, 21(3), pp. 467–474. doi: 10.1007/s12350-014-9858-8.

Bailey, D. L. *et al.* (2005) *Positron Emission Tomography: Basic Sciences*. London: Springer-Verlag.

Bailey, D. L. *et al.* (2014) *Nuclear Medicine Physics*. Vienna: International Atomic Energy Agency. doi: 10.1118/1.3611048.

Bettinardi, V. *et al.* (2011) 'Physical Performance of the new hybrid PETCT Discovery-690', *Medical Physics*, 38(10), pp. 5394–5411. doi: 10.1118/1.3635220.

Boellaard, R. (2009) 'Standards for PET Image Acquisition and Quantitative Data Analysis', *Journal of Nuclear Medicine*, 50(Suppl_1), pp. 11S-20S. doi: 10.2967/jnumed.108.057182.

Bom, M. J. *et al.* (2019) 'Impact of individualized segmentation on diagnostic performance of quantitative positron emission tomography for haemodynamically significant coronary artery disease', *European Heart Journal Cardiovascular Imaging*, 20(5), pp. 525–532. doi: 10.1093/ehjci/jey201.

Byrne, C. *et al.* (2021) 'Test–retest repeatability and software reproducibility of myocardial flow measurements using rest/adenosine stress Rubidium-82 PET/CT with and without motion correction in healthy young volunteers', *Journal of Nuclear Cardiology*, 28(6), pp. 2860–2871. doi: 10.1007/s12350-020-02140-1.

Caribé, P. R. R. V. *et al.* (2019) 'Noise reduction using a Bayesian penalized-likelihood reconstruction algorithm on a time-of-flight PET-CT scanner', *EJNMMI Physics*, 6(1). doi: 10.1186/s40658-019-0264-9.

Cherry, S. R., Sorenson, J. A. and Phelps, M. E. (2012) 'Radiation Detectors', in *Physics in Nuclear Medicine*. Elsevier Saunders. doi: 10.1016/B978-1-4160-5198-5.00007-1.

Chiribiri, A. *et al.* (2013) 'Perfusion phantom: An efficient and reproducible method to simulate myocardial first-pass perfusion measurements with cardiovascular magnetic resonance', *Magnetic Resonance in Medicine*, 69(3), pp. 698–707. doi: 10.1002/mrm.24299.

Christensen, N. L. and Tolbod, L. P. (2017) 'Bayesian Penalized Likelihood Image Reconstruction (Q.Clear) in 82Rb Cardiac PET: Impact of Count Statistics', *European Association of Nuclear Medicine Annual Congress, Vienna, Austria, 21/10/2017 - 25/10/2017*. doi: 10.1007/s00259-017-3822-1.

Danad, I. *et al.* (2014) 'Quantitative assessment of myocardial perfusion in the detection of significant coronary artery disease: Cutoff values and diagnostic accuracy of quantitative [15O]H2O PET imaging', *Journal of the American College of Cardiology*, 64(14), pp. 1464–1475. doi: 10.1016/j.jacc.2014.05.069.

deKemp, R. A. *et al.* (2008) '3D List-mode Cardiac PET for simultaneous quantification of myocardial blood flow and ventricular function', *IEEE Nuclear Science Symposium Conference Record*, pp. 5215–5218. doi: 10.1109/NSSMIC.2008.4774409.

van Dijk, J. D. *et al.* (2019) 'Comparison of maximal Rubidium-82 activities for myocardial blood flow quantification between digital and conventional PET systems', *Journal of Nuclear Cardiology*, 26(4), pp. 1286–1291. doi: 10.1007/s12350-017-1156-9.

Dilsizian, V. *et al.* (2016) *ASNC imaging guidelines/SNMMI procedure standard for positron emission tomography (PET) nuclear cardiology procedures*, *Journal of Nuclear Cardiology*. doi: 10.1007/s12350-016-0522-3.

El Fakhri, G. *et al.* (2009) 'Reproducibility and accuracy of quantitative myocardial blood flow assessment with 82Rb PET: Comparison with 13N-ammonia PET', *Journal of Nuclear Medicine*, 50(7), pp. 1062–1071. doi: 10.2967/jnumed.104.007831.

Fiechter, M. *et al.* (2012) 'Diagnostic value of 13N-ammonia myocardial perfusion PET: Added value of myocardial flow reserve', *Journal of Nuclear Medicine*, 53(8), pp. 1230–1234. doi: 10.2967/jnumed.111.101840.

Gabrani-Juma, H. *et al.* (2017) 'Validation of a Multimodality Flow Phantom and Its Application for Assessment of Dynamic SPECT and PET Technologies', *IEEE Transactions on Medical Imaging*, 36(1), pp. 132–141. doi: 10.1109/TMI.2016.2599779.

GE Healthcare (2017) 'Lightburst Digital Detector Workflow'.

Germano, G., Berman, D. S. and Slomka, P. (2016) 'Technical Aspects of Cardiac PET Imaging and Recent Advances', *Cardiology Clinics*, 34(1), pp. 13–23. doi: 10.1016/j.ccl.2015.07.015.

Germino, M. *et al.* (2016) 'Quantification of myocardial blood flow with 82Rb: Validation with 15O-water using time-of-flight and point-spread-function modeling', *EJNMMI Research*, 6(1). doi: 10.1186/s13550-016-0215-6.

Globus, M. and Grinyov, B. (2006) *Scintillation detectors for medical and biology applications: Materials, design and light collection conditions*, *NATO Security through Science Series B: Physics and Biophysics*. doi: 10.1007/1-4020-5093-3_9.

Grant, A. M. *et al.* (2016) 'NEMA NU 2-2012 performance studies for the SiPM-based ToF-PET component of the GE SIGNA PET/MR system', *Medical Physics*, 43(5), pp. 2334–2343. doi: 10.1118/1.4945416.

Grönman, M. *et al.* (2021) 'Assessment of myocardial viability with [15O]water PET: A validation study in experimental myocardial infarction', *Journal of Nuclear Cardiology*, 28(4), pp. 1271–1280. doi: 10.1007/s12350-019-01818-5.

Harms, H. J. *et al.* (2014) 'Comparison of clinical non-commercial tools for automated quantification of myocardial blood flow using oxygen-15-labelled water PET/CT', *European Heart Journal Cardiovascular Imaging*, 15(4), pp. 431–441. doi: 10.1093/ehjci/jet177.

Heinle, I. and Siraj, Q. H. (2009) 'Artefacts and pitfalls in myocardial perfusion imaging', *Integrating Cardiology for Nuclear Medicine Physicians: A Guide to Nuclear Medicine Physicians*, pp. 325–342. doi: 10.1007/978-3-540-78674-0_28.

Hesse, B. *et al.* (2008) *EANM/ESC guidelines for radionuclide imaging of cardiac function*, *European Journal of Nuclear Medicine and Molecular Imaging*. doi: 10.1007/s00259-007-0694-9.

Hsu, D. F. C. *et al.* (2017) 'Studies of a Next-Generation Silicon-Photomultiplier–Based Time-of-Flight PET/CT System', *Journal of Nuclear Medicine*, 58(9), pp. 1511–1518. doi: 10.2967/jnumed.117.189514.

Iida, H. *et al.* (1988) 'Measurement of absolute myocardial blood flow with H2150 and dynamic positron emission tomography: strategy for quantification in relation to the partial volume effect', *Circulation*, 78(1), pp. 104–115. doi: 10.1161/01.CIR.78.1.104.

Iida, H. *et al.* (1991) 'Myocardial Tissue Fraction - Correction for Partial Volume Effects and Measure of Tissue Viability', *Journal of Nuclear Medicine*, 32(11), pp. 2169–2175.

Iida, H. *et al.* (1992) 'Use of the left ventricular time-activity curve as a noninvasive input function in dynamic oxygen-15-water positron emission tomography.', *Journal of nuclear medicine : official publication, Society of Nuclear Medicine*, 33(9), pp. 1669–1677.

Johansson, B. L. *et al.* (2004) 'C-peptide improves adenosine-induced myocardial vasodilation in type 1 diabetes patients', *American Journal of Physiology - Endocrinology and Metabolism*, 286(1 49-1), pp. 14–19. doi: 10.1152/ajpendo.00236.2003.

Kajander, S. *et al.* (2010) 'Cardiac positron emission tomography/computed tomography imaging accurately detects anatomically and functionally significant coronary artery disease', *Circulation*, 122(6), pp. 603–613. doi: 10.1161/CIRCULATIONAHA.109.915009.

Karp, J. S. *et al.* (2008) 'Benefit of time-of-flight in PET: Experimental and clinical results', *Journal of Nuclear Medicine*, 49(3), pp. 462–470. doi: 10.2967/jnumed.107.044834.

Kaufmann, P. A. *et al.* (1999) 'Assessment of the reproducibility of baseline and hyperemic myocardial blood flow measurements with 15O-labeled water and PET', *Journal of Nuclear Medicine*, 40(11), pp. 1848–1856.

Kero, T. *et al.* (2017) 'Quantitative myocardial blood flow imaging with integrated time-of-flight PET-MR', *EJNMMI Physics*, 4(1), pp. 1–13. doi: 10.1186/s40658-016-0171-2.

Klein, R. *et al.* (2018) 'Consistent tracer administration profile improves test–retest repeatability of myocardial blood flow quantification with 82Rb dynamic PET imaging', *Journal of Nuclear Cardiology*, 25(3), pp. 929–941. doi: 10.1007/s12350-016-0698-6.

Knaapen, P. and Lubberink, M. (2008) 'Cardiac positron emission tomography: Myocardial perfusion and metabolism in clinical practice', *Clinical Research in Cardiology*, 97(11), pp. 791–796. doi: 10.1007/s00392-008-0662-9.

Knuuti, J. *et al.* (2009) 'Quantification of myocardial blood flow will reform the detection of CAD', *Journal of Nuclear Cardiology*, 16(4), pp. 497–506. doi: 10.1007/s12350-009-9101-1.

Koepfli, P. *et al.* (2004) 'CT attenuation correction for myocardial perfusion quantification using a PET/CT hybrid scanner', *Journal of Nuclear Medicine*, 45(4), pp. 537–542.

Koopman, D. *et al.* (2019) 'SUV variability in EARL-accredited conventional and digital PET', *EJNMMI Research*, 9(1). doi: 10.1186/s13550-019-0569-7.

Lassen, M. L. *et al.* (2020) '3D PET/CT 82Rb PET myocardial blood flow quantification: comparison of half-dose and full-dose protocols', *European Journal of Nuclear Medicine and Molecular Imaging*, IN PRESS.

Lecoq, P. and Gundacker, S. (2021) 'SiPM applications in positron emission tomography: toward ultimate PET time-of-flight resolution', *European Physical Journal Plus*, 136(3), pp. 1–16. doi: 10.1140/epjp/s13360-021-01183-8.

Lederer, C. M., Hollander, J. M. and Perlman, I. (1967) *Table of Isotopes*. 6th edn, *Physics Today*. 6th edn. Wiley. doi: 10.1063/1.3034044.

Lewellen, T. K. *et al.* (1994) 'Investigation of the count rate performance of the General Electric Advance positron emission tomograph', *Nuclear Science Symposium and Medical Imaging Conference, 1994., 1994 IEEE Conference Record*, 3(4), pp. 1169–1173 vol.3. doi: 10.1109/NSSMIC.1994.474637.

Lodge, M. A. (2017) 'Repeatability of SUV in oncologic 18F-FDG PET', *Journal of Nuclear Medicine*, 58(4), pp. 523–532. doi: 10.2967/jnumed.116.186353.

Maaniitty, T. *et al.* (2017) 'Prognostic Value of Coronary CT Angiography With Selective PET Perfusion Imaging in Coronary Artery Disease', *JACC: Cardiovascular Imaging*, 10(11), pp. 1361–1370. doi: 10.1016/j.jcmg.2016.10.025.

Matheoud, R. *et al.* (2017) 'Erratum to: Comparative analysis of iterative reconstruction algorithms with resolution recovery and time of flight modeling for 18F-FDG cardiac PET: A multicenter phantom study (J NUCL CARDIOL, 10.1007/S12350-015-0385-Z)', *Journal of Nuclear Cardiology*, 24(3), p. 1101. doi: 10.1007/s12350-016-0415-5.

Mawlawi, O. R. *et al.* (2019) *PET/CT Acceptance Testing and Quality Assurance*, *Aapm*.

Moccetti, F. and Lindner, J. R. (2019) *Utilizing Contrast Echocardiography in Practice*, *Essential Echocardiography: A Companion to Braunwald's Heart Disease*. Elsevier. doi: 10.1016/B978-0-323-39226-6.00012-6.

Monroy-Gonzalez, A. G. *et al.* (2020) 'Software reproducibility of myocardial blood flow and flow reserve quantification in ischemic heart disease: A 13N-ammonia PET study', *Journal of Nuclear Cardiology*, 27(4), pp. 1225–1233. doi: 10.1007/s12350-019-01620-3.

Moody, J. B. *et al.* (2015) 'Precision and accuracy of clinical quantification of myocardial blood flow by dynamic PET: A technical perspective', *Journal of Nuclear Cardiology*, 22(5), pp. 935–951. doi: 10.1007/s12350-015-0100-0.

Moody, J. B., Ficaro, E. P. and Murthy, V. L. (2020) 'Simplified quantification of PET myocardial blood flow: The need for technical standardization', *Journal of Nuclear Cardiology*, 27(3), pp. 829–832. doi: 10.1007/s12350-018-01497-8.

Morris, E. D. *et al.* (2004) 'Kinetic Modeling in Positron Emission Tomography', *Emission Tomography: The Fundamentals of PET and SPECT*, pp. 499–540. doi: 10.1016/B978-012744482-6.50026-0.

Murthy, V. L. *et al.* (2018) 'Clinical quantification of myocardial blood flow using PET: Joint position paper of the SNMMI cardiovascular council and the ASNC', *Journal of Nuclear Medicine*, 59(2), pp. 273–293. doi: 10.2967/jnumed.117.201368.

Muzik, O. *et al.* (1993) 'Validation of nitrogen-13-ammonia tracer kinetic model for quantification of myocardial blood flow using PET', *Journal of Nuclear Medicine*, 34(1), pp. 83–91.

Nadig, V. *et al.* (2022) 'Hybrid total-body pet scanners—current status and future perspectives', *European Journal of Nuclear Medicine and Molecular Imaging*, 49(2), pp. 445–459. doi: 10.1007/s00259-021-05536-4.

Nammas, W. *et al.* (2021) 'Cardiac perfusion by positron emission tomography', *Clinical Physiology and Functional Imaging*, 41(5), pp. 385–400. doi: 10.1111/cpf.12708.

National Electrical Manufacturers Association (2012) 'Performance Measurements of Positron Emission Tomographs. NEMA Standards publication NU2-2012'.

Nesterov, S. V. *et al.* (2009) 'Myocardial perfusion quantitation with 15O-labelled water PET: High reproducibility of the new cardiac analysis software (Carimas™)', *European Journal of Nuclear Medicine and Molecular Imaging*, 36(10), pp. 1594–1602. doi: 10.1007/s00259-009-1143-8.

Nordström, J. *et al.* (2022) 'Influence of image reconstruction on quantitative cardiac 15 O-water positron emission tomography', *Journal of Nuclear Cardiology*. doi: 10.1007/s12350-022-03075-5.

O' Doherty, J. *et al.* (2017) 'The effect of high count rates on cardiac perfusion quantification in a simultaneous PET-MR system using a cardiac perfusion phantom', *EJNMMI Physics*, 4(1). doi: 10.1186/s40658-017-0199-y.

O'Doherty, J. *et al.* (2017) 'Effect of Bayesian-penalized likelihood reconstruction on [13N]-NH3 rest perfusion quantification', *Journal of Nuclear Cardiology*, 24(1), pp. 282–290. doi: 10.1007/s12350-016-0554-8.

Oikonen, V. (2019) *<http://www.turkupetcentre.net/petanalysis/model_perfusion.html>, accessed 14.6.2023*.

Ollinger, J. M. (1996) 'Model-based scatter correction for fully 3D PET', *Physics in Medicine and Biology*, 41(1), pp. 153–176. doi: 10.1088/0031-9155/41/1/012.

Presotto, L. *et al.* (2015) 'Evaluation of image reconstruction algorithms encompassing Time-Of-Flight and Point Spread Function modelling for quantitative cardiac PET: Phantom studies', *Journal of Nuclear Cardiology*, 22(2), pp. 351–363. doi: 10.1007/s12350-014-0023-1.

Prior, J. O. *et al.* (2012) 'Quantification of myocardial blood flow with 82Rb positron emission tomography: Clinical validation with 15O-water', *European Journal of Nuclear Medicine and Molecular Imaging*, 39(6), pp. 1037–1047. doi: 10.1007/s00259-012-2082-3.

Rahmim, A., Qi, J. and Sossi, V. (2013) 'Resolution modeling in PET imaging: Theory, practice, benefits, and pitfalls', *Medical Physics*, 40(6). doi: 10.1118/1.4800806.

Reader, A. J. and Zaidi, H. (2007) 'Advances in PET Image Reconstruction', *PET Clinics*, 2(2), pp. 173–190. doi: 10.1016/j.cpet.2007.08.001.

Reddin, J. S. *et al.* (2018) 'Performance Evaluation of the SiPM-based Siemens Biograph Vision PET/CT System', *2018 IEEE Nuclear Science Symposium and Medical Imaging Conference, NSS/MIC 2018 - Proceedings*, pp. 1–5. doi: 10.1109/NSSMIC.2018.8824710.

Renaud, J. M. *et al.* (2017) 'Characterization of 3-Dimensional PET Systems for Accurate Quantification of Myocardial Blood Flow', *Journal of Nuclear Medicine*, 58(1), pp. 103–109. doi: 10.2967/jnumed.116.174565.

Reyes, E. (2016) 'Regadenoson stress for myocardial perfusion imaging', *Future Cardiology*, 12(1), pp. 59–67. doi: 10.2217/fca.15.70.

Reynés-Llompart, G. *et al.* (2017) 'Performance characteristics of the whole-body discovery IQ PET/CT system', *Journal of Nuclear Medicine*, 58(7), pp. 1155–1161. doi: 10.2967/jnumed.116.185561.

Riegler, G. *et al.* (2017) 'Influence of PET reconstruction technique and matrix size on qualitative and quantitative assessment of lung lesions on [18F]-FDG-PET: A prospective study in 37 cancer patients', *European Journal of Radiology*, 90, pp. 20–26. doi: 10.1016/j.ejrad.2017.02.023.

Ross, S. (2014) 'Q.Clear', *GE Healthcare*. Available at: www.gehealthcare.com.

Sciagrà, R. *et al.* (2021) 'EANM procedural guidelines for PET/CT quantitative myocardial perfusion imaging', *European Journal of Nuclear Medicine and Molecular Imaging*, 48(4), pp. 1040–1069. doi: 10.1007/s00259-020-05046-9.

Shi, X. *et al.* (2018) 'Comparison among Reconstruction Algorithms for Quantitative Analysis of 11 C-Acetate Cardiac PET Imaging', *Contrast Media and Molecular Imaging*, 2018. doi: 10.1155/2018/9193403.

Siekkinen, R. *et al.* (2019) 'Study of Repeatability of a Novel PET Flow Phantom', in *IEEE Nuclear Science Symposium and Medical Imaging Conference (NSS/MIC), Manchester, United Kingdom*. IEEE, pp. 11–14.

Van Sluis, J. *et al.* (2019) 'Performance characteristics of the digital biograph vision PET/CT system', *Journal of Nuclear Medicine*, 60(7), pp. 1031–1036. doi: 10.2967/jnumed.118.215418.

Stearns, C. W. *et al.* (2004) 'Random coincidence estimation from single event rates on the Discovery ST PET/CT scanner', *2003 IEEE Nuclear Science Symposium. Conference Record (IEEE Cat. No.03CH37515)*, pp. 3067–3069. doi: 10.1109/NSSMIC.2003.1352545.

Suda, M. *et al.* (2016) 'The reproducibility of time-of-flight PET and conventional PET for the quantification of myocardial blood flow and coronary flow reserve with 13N-ammonia', *Journal of Nuclear Cardiology*, 23(3), pp. 457–472. doi: 10.1007/s12350-015-0074-y.

Surti, S. *et al.* (2006) 'Investigation of time-of-flight benefit for fully 3-D PET', *IEEE Transactions on Medical Imaging*, 25(5), pp. 529–538. doi: 10.1109/TMI.2006.871419.

Surti, S. (2015) 'Update on time-of-flight PET imaging', *Journal of Nuclear Medicine*, 56(1), pp. 98–105. doi: 10.2967/jnumed.114.145029.

Tong, S., Alessio, A. M. and Kinahan, P. E. (2010) 'Image reconstruction for PET/CT scanners: Past achievements and future challenges', *Imaging in Medicine*, 2(5), pp. 529–545. doi: 10.2217/iim.10.49.

Trägårdh, E. *et al.* (2019) 'Impact of acquisition time and penalizing factor in a block-sequential regularized expectation maximization reconstruction algorithm on a Si-photomultiplier-based PET-CT system for 18F-FDG', *EJNMMI Research*, 9(1). doi: 10.1186/s13550-019-0535-4.

Vandenberghe, S. *et al.* (2016) 'Recent developments in time-of-flight PET', *EJNMMI Physics*, 3(1). doi: 10.1186/s40658-016-0138-3.

Vandendriessche, D. *et al.* (2019) 'Performance characteristics of silicon photomultiplier based 15-cm AFOV TOF PET/CT', *EJNMMI Physics*, 6(1). doi: 10.1186/s40658-019-0244-0.

Walker, M. D. *et al.* (2009) 'Optimization of the Injected Activity in Dynamic 3D PET: A Generalized Approach Using Patient-Specific NECs as Demonstrated by a Series of 15O-H2O Scans', *Journal of Nuclear Medicine*, 50(9), pp. 1409–1417. doi: 10.2967/jnumed.109.062679.

Walter, G. G. (1986) ‘Compartmental modelling and tracer kinetics’, *Mathematical Biosciences*, 79(1), pp. 117–118. doi: 10.1016/0025-5564(86)90021-0.

Watson, C. C., Newport, D. and Casey, M. E. (1996) ‘A single scatter simulation technique for scatter correction in 3D PET’, *Three-Dimensional Image Reconstruction in Radiation and Nuclear Medicine*, pp. 255–268. doi: 10.1007/978-94-015-8749-5_18.

Wyss, C. A. *et al.* (2003) ‘Bicycle exercise stress in PET for assessment of coronary flow reserve: repeatability and comparison with adenosine stress.’, *Journal of nuclear medicine : official publication, Society of Nuclear Medicine*, 44(2), pp. 146–154.

Ziadi, M. C. (2017) ‘Myocardial flow reserve (MFR) with positron emission tomography (PET)/computed tomography (CT): Clinical impact in diagnosis and prognosis’, *Cardiovascular Diagnosis and Therapy*, 7(2), pp. 206–218. doi: 10.21037/cdt.2017.04.10.

TURUN
YLIOPISTO
UNIVERSITY
OF TURKU

Painosalama, Turku, Finland 2023

ISBN 978-951-29-9419-9 (PRINT)
ISBN 978-951-29-9420-5 (Online)
ISSN 0355-9483 (Print)
ISSN 2343-3213 (Online)